Christian Binter

Multi-Point 3D Velocity Vector Encoding of Blood Flow

Master thesis

Institute of Medical Engineering
Graz University of Technology
Kronesgasse 5, A-8010 Graz
Head: Univ.-Prof. Dipl.-Ing. Dr. techn. Rudolf Stollberger

Supervisor: Univ.-Prof. Dipl.-Ing. Dr. techn. Rudolf Stollberger
and
Univ. Prof. Dr. Sebastian Kozerke, Institute of Biomedical Engineering,
University and ETH Zürich

Evaluator: Univ.-Prof. Dipl.-Ing. Dr. techn. Rudolf Stollberger

Graz, May 2011

EIDESSTATTLICHE ERKLÄRUNG

Ich erkläre an Eides statt, dass ich die vorliegende Arbeit selbstständig verfasst, andere als die angegebenen Quellen/Hilfsmittel nicht benutzt und die den benutzten Quellen wörtlich und inhaltlich entnommenen Stellen als solche kenntlich gemacht habe.

Graz, am …… ……..

(Unterschrift)

STATUTORY DECLARATION

I declare that I have authored this thesis independently, that I have not used other than the declared sources / resources and that I have explicitly marked all material which has been quoted either literally or by content from the used sources.

…… ……..

date (signature)

Multi-Point 3D Velocity Vector Encoding of Blood Flow

Magnetic Resonance Imaging offers the possibility to non-invasively assess blood flow. Different diseases in the cardiovascular system are closely linked to pathological flow and information about the flow can be employed to diagnose and investigate such diseases.

There exist well-established methods to measure the mean velocity of blood flow, and recently a technique to assess turbulence intensity was proposed. All these approaches suffer from high sensitivity to chosen scan parameters and noise. In this work a new method is presented which combines highly accelerated measurements with a Bayesian approach. Phase-Contrast Magnetic Resonance Imaging is employed using different encoding velocities. Coherent motion leads to a velocity depending phase, and velocity fluctuations caused by turbulence lead to a decrease in signal magnitude. These effects in combination with statistical methods result in a posterior probability of the mean velocity and turbulence intensity. This probability is then maximized to obtain an estimate of these parameters.

The technique proposed has shown promising results regarding the accuracy compared to conventional methods, especially in the low SNR regime. The practicability was demonstrated using in vitro as well as in vivo measurements, including pathological flow situations. Further investigation is required to improve speed and to validate the results of turbulence intensities.

Keywords: Magnetic Resonance Imaging, phase-contrast velocity mapping, turbulence intensity, Bayesian approach, accelerated imaging

Mehrpunkt 3D Geschwindigkeitsvektor-Kodierung des Blutflusses

Die Magnetresonanztomographie (MRT) ermöglicht die nicht-invasive Messung des Blutflusses. Verschiedene Erkrankungen des Herz-Kreislauf-Systems stehen in Relation zu Veränderungen des Flusses und entsprechend bieten Messmethoden zur Bestimmung von Blutflussgeschwindigkeiten und -vektorfeldern wichtige Information zur Diagnose und Untersuchung solcher Krankheiten.

MRT-Methoden zur Messung der mittleren Geschwindigkeit des Blutflusses sind mittlerweile gut etabliert. Darüber hinaus hat die Entwicklung von Verfahren zur Bestimmung der Turbulenzintenstität großes Interesse hervorgerufen, da damit signifikante Veränderungen der Hämodynamik detektiert werden könnten. Die Genauigkeit derzeitiger Implementationen ist jedoch stark von der Wahl verschiedener Messparameter und vom Messrauschen abhängig.

In dieser Arbeit wird eine neue Methode vorgestellt, welche stark beschleunigte Messverfahren mit einem Bayes‘schen Ansatz kombiniert. Hierzu kommen Phasenkontrast MRT-Messungen mit verschiedenen Kodiergeschwindigkeiten zur Anwendung. Auf Grundlage derer können Turbulenzintensitäten und Geschwindigkeiten berechnet werden. Kohärenter Blutfluss resultiert in einer Signalphase, die linear von der Geschwindigkeit abhängt. Im Gegensatz dazu führt Turbulenz oder Geschwindigkeitsfluktuation zu einer Abnahme der Signalmagnitude. In Verbindung mit statistischen Methoden ergeben diese Effekte eine a-posteriori Wahrscheinlichkeit der mittleren Geschwindigkeit und der Turbulenzintensität. Durch Maximierung dieser Wahrscheinlichkeit können Schätzungen dieser Parameter bestimmt werden.

Das in dieser Arbeit implementierte Verfahren zeigt vielversprechende Ergebnisse bezüglich Genauigkeit im Vergleich zu konventionellen Methoden, insbesondere im Bereich kleiner Signal-zu-Rausch Werte. Die Anwendbarkeit der entwickelten Technik wurde in-vitro als auch in-vivo in Patienten mit Klappenprothesen überprüft. Zukünftige Untersuchungen folgen, um die klinischen Nutzen unter Beweis zu stellen.

Schlagwörter: Magnetresonanztomographie, Phasenkontrast-Geschwindigkeitsmessung, Turbulenzintensität, Bayes‘sche Statistik, beschleunigte Bildgebung

Table of Contents

1 Introduction

Cardiovascular diseases (CVD) are the leading cause of death in Western countries, responsible for more than 40% of all fatalities in Europe [1]. Many pathologies of the circulatory system are accompanied by altered blood flow. Therefore knowledge about the flow conditions inside the human body can lead to a better understanding and more accurate prediction and diagnosis of CVD.

In today's clinical routine, the assessment of blood flow velocities is usually performed using Doppler sonography [2]. It is a quick, non-invasive method, although its application is limited to regions with adequate acoustic windows, and three dimensional velocity measurements are very limited. Invasive methods include hot-film anemometry [3] and Doppler sonography using invasive ultrasound transceivers. Because of the higher risks and discomfort of invasive methods compared to the actual diagnostic benefits, their use is mainly limited to research and not feasible in clinical practice.

Another non-invasive imaging modality for flow measurements is Magnetic Resonance Imaging (MRI). The idea behind Phase-Contrast (PC) velocity measurements was introduced in the 1950s [4]. In-vivo application started more than 20 years later [5]. Because of long scan times and the required post-processing, its use in cardiac imaging had been limited. Improvements in hardware in combination with new and faster acquisition techniques have led to an increased interest in using PC measurements for cardiovascular studies, resulting in a number of proposed applications for this technique [6].

Detailed quantification of blood flow can be used to assess cardiac output, diastolic function and the severity of valvular diseases. Dysfunctional heart valves can lead to abnormal flow patterns like regurgitation or jet-like behavior, and quantification of these abnormalities is essential in deciding about interventional measures. Other applications of velocity measurements include evaluation of congenital shunt lesions [6], where pathological flow between pulmonary and systemic circulation is evaluated, or diagnosis of aortic dissection, where flow patterns can be used to distinguish false and true lumen [7].

It has been suggested that disturbed flow and accompanying abnormal wall shear stresses are involved in the pathogenesis of atherosclerosis [8], giving an explanation for the

increased occurrence at specific locations like bifurcations or sharp bends. A tool which could provide detailed information about flow patterns would help to more accurately determine the risk resulting from atherosclerotic lesions for each patient individually.

To assess the forces on the vessel walls, not only the velocity vector field of the flow can be considered, but high turbulence intensities in the vicinity of vessel walls can also be an indicator for pathological flow patterns. Increased turbulence not only results in altered wall shear stresses but also in higher stresses on platelets and erythrocytes, leading to a release of enzymes which play a key role in thrombus formation [9]. In physiological flow conditions turbulence rarely occurs, but valvular stenosis or artificial heart valves can change the flow severely [10]. Therefore turbulence assessment can be useful in optimizing the design of valve prosthetics.

The number of methods to quantify turbulence in vivo is quite limited, including mentioned hot-film anemometry (invasive) and ultrasound (non-invasive). Another technique is Particle Image Velocimetry (PIV), but its use is restricted to in-vitro measurements [11]. A general description of the effects of turbulence on the MRI signal has been stated 20 years ago [12], but only recently an applicable method of in-vivo measurements has been proposed and implemented by Dyverfeldt et al [13].

The acquisition of velocity vector fields and turbulence maps (more specifically: Turbulent Kinetic Energy (TKE) maps) at the same time can be realized using the technique Dyverfeldt et al. proposed. However, in order to achieve maximum sensitivity of turbulence measurements, an encoding or aliasing velocity (VENC) inversely proportional to the expected turbulence intensity has to be used. Accordingly, the method requires an estimate of the amount of turbulence to expect, and its accuracy varies with the actual TKE values. Also a VENC not high enough can lead to ambiguous velocity measurements because of phase aliasing.

For more accurate acquisition of the velocity vector field several improvements have been proposed, such as a variable encoding velocity over the heart cycle [14] and unwrapping of measurements with low VENC using scans with higher VENC as a reference [15] to achieve a higher Velocity-to-Noise Ratio (VNR).

Xing et al [16] demonstrated the use of a Bayesian statistical method in combination with multiple encoding velocities for flow and diffusion NMR measurements, which enables a more accurate determination of velocities than using conventional Phase-Contrast (PC)

imaging. In this work this principle is developed further, and a framework for simultaneous acquisition of TKE and velocity information is presented. It will be shown that this approach can lead to more accurate information about both velocities and turbulence per unit scan time when compared to conventional methods. The technique will be demonstrated using simulated and in-vitro data as well as in-vivo results, examining the flow patterns in the heart and aorta of healthy volunteers as well as pathological cases. Two artificial aortic valves will be compared in-vitro, and in-vivo data from one patient with such a valve will be presented.

2 Methods and Fundamental Concepts

This chapter gives a short introduction into the principles of Magnetic Resonance Imaging and should provide an overview of flow and turbulence measurements. Also the method of accelerated imaging used in this work is described, and the adapted Bayesian analysis for parameter estimation is illustrated in detail.

2.1 Principles of MRI

Magnetic Resonance Imaging (MRI) uses the inherent magnetic properties of atomic nuclei to extract functional and anatomical information and convert them into images. Several nuclei possess an angular momentum called spin. These nuclei interact with external magnetic fields, other nuclei and the electrons surrounding them. This chapter only offers a brief introduction to signal generation and image formation, a more detailed description can be found in i.e. [17] .

2.1.1 Microscopic Mechanisms

If nuclei with spin ½ are brought into a static external magnetic field $\mathbf{B_0}$, their z-component aligns either parallel or antiparallel with this field. Because the parallel state is energetically more favorable, transitions between the anti-parallel and parallel states are only possible via emission or absorption of some form of energy. Such transitions can be induced via a radiofrequency (RF) magnetic field at the specific resonance frequency (Larmor frequency ω_0) of the nuclei. This frequency is linked to the angular momentum **J** and the resulting magnetic moment $\boldsymbol{\mu}$ via the gyromagnetic ratio γ:

$$\omega_0 = \gamma B_0 = \frac{\mu}{J} B_0 \qquad \text{(eq. 1)}$$

In clinical use, mostly relevant are ^{1}H-protons with a gyromagnetic ratio γ/2π of 42.58 MHz/T, but for special applications nuclei like ^{19}F or ^{31}P can also be used.

If macroscopic packets of spins are considered, classical laws of physics can be applied. The summed magnetic moment vectors of the nuclei in a voxel result in a net magnetization vector **M**. The torque acting on a magnetic moment μ in a magnetic field B is given by the

vector product **μ** x **B**, and consideration of the interactions of spins with their surrounding results in the Bloch equation (eq. 2):

$$\frac{d\boldsymbol{M}}{dt} = \gamma(\boldsymbol{M} \times \boldsymbol{B}) - \frac{M_x}{T_2}\boldsymbol{e_x} - \frac{M_y}{T_2}\boldsymbol{e_y} - \frac{M_z - M_0}{T_1}\boldsymbol{e_z} \qquad \text{(eq. 2)}$$

The tissue dependent terms T_1 and T_2 describe the longitudinal and transversal relaxation times, respectively. These result from spin-spin interactions (T_2) or spin-lattice interactions (T_1), and are the basis for different contrast mechanisms of various pulse sequences.

The transversal component M_{xy} precessing around the z-axis induces a signal proportional to the magnitude of M_{xy} in the receiver coil, which is then recorded and processed.

2.1.2 Spatial Encoding

It is desirable to be able to exactly determine the spatial origin of the signal which is induced in a coil. This is possible using different magnetic fields added to the main magnetic field B_0, called *gradient field*s or for short *gradients*. These gradient fields have the same direction as the B_0 field and the magnetic flux varies linearly along the spatial axes (Fig. 2.1a).

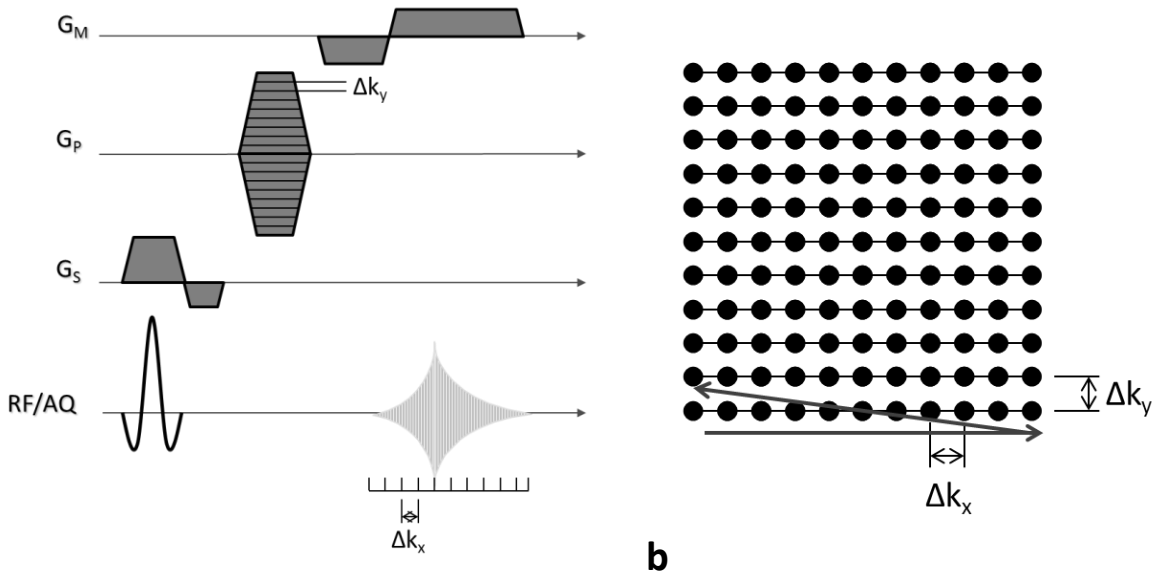

Fig. 2.1: a) 2D Fourier Pulse Sequence used for spatial encoding, b) corresponding k-space.

The first spatial dimension z is encoded using a “slice selection gradient” G_S. This gradient linearly varies over the z-axis and is applied during the excitation of the nuclei via an RF

pulse. Because of the resulting different Larmor frequencies along that axis, a pulse with a certain bandwidth only excites a limited slab or slice.

The second dimension, here y, is then resolved using a phase-encoding gradient G_P. By applying this gradient after the excitation for the duration T_y, the spins precess with different frequencies and therefore accumulate a phase depending on their position y:

$$\phi(G_y, y) = \gamma y \int_0^{T_y} G_P(t)\, dt = \gamma y G_P T_y \qquad \text{(eq. 3)}$$

The gradient G_M for the third dimension x is switched on during registration of the signal, causing a spatially varying frequency shift ω_1 in one direction:

$$\omega_1(G_x, x) = \gamma G_M x \qquad \text{(eq. 4)}$$

The signal s at time t can then be expressed as a combination of frequency and phase:

$$s(t) \propto \iint \rho(x, y, z) e^{i(\omega_1(G_M, x)t + \Phi(G_P, y))} dx dy \qquad \text{(eq. 5)}$$

with ρ being the proton density at position (x, y, z).

Introducing two new variables, $k_x = \gamma \int_0^t G_P(\tau) d\tau$ and $k_y = \gamma \int_0^{T_y} G_P(t)\, dt$, eq. 5 becomes

$$s(z, k_x, k_y) \propto \iint \rho(x, y, z) e^{i(k_x x + k_y y)} dx dy \qquad \text{(eq. 6)}$$

It can be seen, that the signals for a slice correspond to the 2D Fourier transform of the proton density.

Using the two new variables, a new formalism called k-space can be introduced. The discretized signals acquired for every k_x/k_y step are recorded and stored in a matrix for all the slices (Fig. 2.1b), on which an inverse 2D DFT can be applied to recover the image (Fig. 2.2).

It can be seen that during every repetition of the pulse sequence, one line in k-space is acquired. Therefore the acquisition time mainly depends on repetition time TR and the number of k_y steps, as well as on the number of slices. So any method targeting faster imaging will mainly target the phase- and slice-encoding directions, as will be discussed in section 2.4.

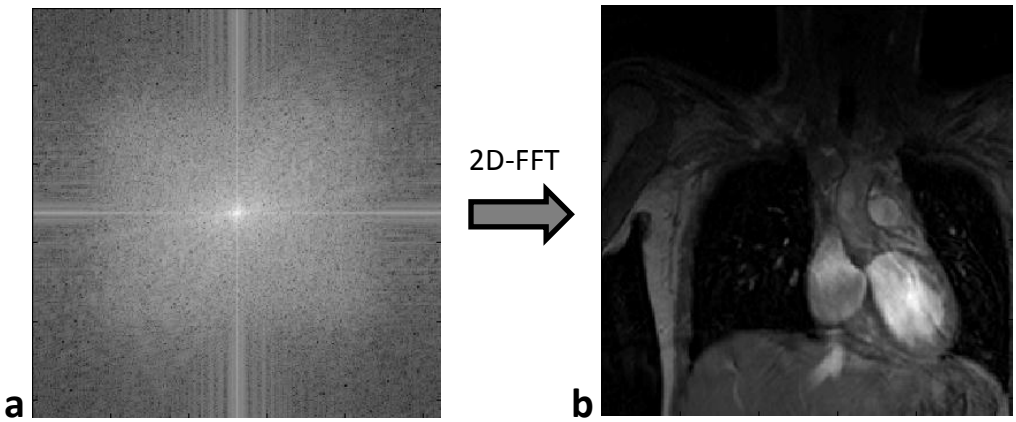

Fig. 2.2: a) Example of an acquired k-space (magnitude, logarithm taken) and b) corresponding magnitude image.

2.1.3 Noise considerations

A limiting factor in MRI is noise. Apart from artifacts originating from body motion, field inhomogenities or external RF fields, the most prominent source of noise is the measured object itself. Thermal agitation of charges in the object induce a noise voltage in the receiver coil. Accordingly the object may be represented by a resistance. The standard deviation of noise voltage induced in the receiver coil can be shown to be proportional to the square root of the equivalent object resistance, receiver bandwidth and temperature [18, 19]. This thermal noise with a Gaussian distribution adds to the signal in both real and imaginary channel.

The principal measure of noise in MRI is the signal-to-noise-ratio SNR:

$$SNR = \frac{A}{\sigma} \qquad \text{(eq. 7)}$$

where A is the amplitude of the signal, and σ is the standard deviation of the noise. Usually those two values are measured using the magnitude image, where the definition of SNR has to change slightly because the noise follows a Rayleigh-distribution with a variance σ^2_m in areas with only background signal [20]:

$$SNR = \frac{A}{\sqrt{\frac{\sigma_m^2}{2 - 0.5\pi}}} \qquad \text{(eq. 8)}$$

If a Gaussian distribution is assumed, the calculation of standard deviation using just the square root of the variance will lead to an underestimation of noise power by up to 35%.

2.2 Flow Encoding

With MRI, not only anatomical information can be acquired, but also functional imaging is possible. One example is the measurement of flow, where the movement of spins during acquisition can be quantified. The most prominent techniques utilize a spatially dependent gradient to induce a phase shift relative to the change in position.

2.2.1 Phase Contrast Velocity Encoding

As mentioned before, a spin in a spatially dependent gradient G accumulates a phase according to eq. 3:

$$\phi(x) = \gamma \int_0^t G_y(\tau) x(\tau)\, d\tau \qquad \text{(eq. 9)}$$

Here the 1-dimensional case is considered, but it can easily be expanded to 3D using measurements for each direction. A Taylor series expansion of x(τ) results in [21]

$$\phi(x) = \phi_0 + \gamma \sum_{n=0}^{\infty} \frac{x^{(n)}}{n!} \int_0^t G(\tau)\tau^n d\tau \qquad \text{(eq. 10)}$$

with $x^{(n)}$ being the n-th derivative of x with respect to time τ. Terminating the series after n=2 and using the fact that $x^{(1)}$ equals the velocity v, as well as $x^{(2)}$ equals acceleration a, eq. 10 yields

$$\phi(x) = \phi_0 + \gamma x \int_0^t G(\tau) d\tau + \gamma v \int_0^t G(\tau)\tau d\tau + \gamma \frac{a}{2} \int_0^t G(\tau)\tau^2 d\tau \qquad \text{(eq. 11)}$$

The term $\int_0^t G(\tau)\tau^n d\tau$ is called the n-th gradient moment m_n. It can be seen that for a flow encoding gradient G the optimal gradient area (= m_0) is 0, because then stationary spins do not acquire any additional phase. An example would be a bipolar gradient with two lobes with equal area (see used pulse sequence in Fig. 2.3).

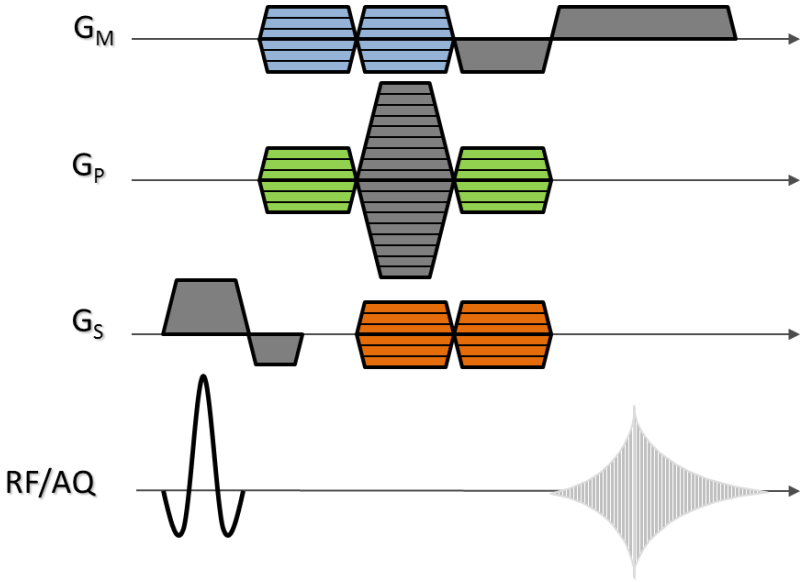

Fig. 2.3: Used Pulse Sequence for flow encoding with different k_v steps. The different flow encoding gradients for three directions are displayed in color, with lines marking the different k_v steps.

Eq. 11 also shows that every imaging gradient results in a phase effect due to motion, leading to unwanted artifacts or signal misregistration. For this purpose, special flow compensating gradients have been developed [22]. For flow measurements, the phase induced by motion is desired. Every velocity measurement is also influenced by acceleration and other higher terms of motion, but their effect on the phase is small compared to that of linear motion.

The term Φ_0 is an arbitrary background phase, originating from field inhomogeneities. It is independent of the gradient and can be compensated by acquiring two measurements with different first gradient moment m_1 and following phase subtraction. Such a reference image, for example with $m_1=0$ can be acquired once and then used for all 3 directions.

The resulting equation for the signal, with acceleration ignored, is given by

$$S(v) = S_0 e^{i(v\gamma m_1+\Phi_0)} = S_0 e^{i(vk_v+\Phi_0)} \qquad \text{(eq. 12)}$$

Here a new formalism similar to k-space is introduced – $k_v=\gamma m_1$, which will be used later on.

An important parameter in phase contrast flow measurements is the aliasing velocity VENC, depending on the difference in first gradient moments $|\Delta m_1|$:

$$VENC = \frac{\pi}{\gamma|\Delta m_1|} = \frac{\pi}{k_{v2} - k_{v1}} \quad \text{(eq. 13)}$$

A velocity of ±VENC results in a phase shift of ±π, making it the maximum resolvable velocity. The aliasing velocity has a large impact on the accuracy of the measurements, because the phase errors originating from Gaussian noise will always have a standard deviation σ_{ph} which is largely independent from the gradient strength. These phase errors will then be mapped to different velocities according to

$$\sigma_{v,error}(VENC) = \frac{\sigma_{ph} VENC}{\pi} \quad \text{(eq. 14)}$$

So higher VENCs will lead to higher standard deviations of the measured velocity, but VENCs which are set too low will result in phase wraps.

To objectively compare the quality of velocity measurements, the velocity to noise ratio VNR is introduced:

$$VNR = \frac{V}{\sigma_{v,error}} \quad \text{(eq. 15)}$$

where V is the average velocity in an area of the image.

2.2.2 k_v-space and acquisition schemes

For determination of the mean velocity in a voxel, a minimum of two measurements with different first gradient moments m_1 is necessary. In k_v-space notation, two points in the k_v-space have to be acquired. From this point on, this will be called 2-point phase contrast (PC). If the reference segment is not flow encoded (k_v=0), it can be used for all three direction in the 3D case. Then only 4 steps result in a 3-dimensional velocity vector field. Again, the VENCs have to be chosen higher than every occurring velocity. Such a scan can be done in a relatively short time, but the resulting VNR very much depends on the chosen VENC, and varies throughout the heart cycle.

If acquisition time is considered, Fourier Velocity Encoding (FVE) involving many k_v encoding steps is clearly limited. Here a full k_v-space is acquired, and Fourier transform not only gives us the mean velocity in a voxel, but also the velocity distribution. The velocity resolution is inversely proportional to the number of encoding steps N. With current

technology, a high number of k_v steps would result in a prohibitively long scan time, especially in when encoding is performed in three dimensions. Consequently in-vivo measurements are not feasible, even when acceleration techniques are employed.

A compromise between accuracy and scan time is a 3-point PC measurement, as suggested by Lee et al. [15]. Here three steps in k_v-space are acquired, one reference segment, one with a relatively high k_v (=$VENC_{low}$) which results in an aliased image, and a third segment (high VENC) without phase wraps, which is consequently used to unwrap the aliased image according to

$$V = V_{low} + 2VENC_{low}\ N.I.\left(\frac{V_{high} - V_{low}}{2VENC_{low}}\right) \qquad \text{(eq. 16)}$$

where N.I. is the nearest integer-function, and V_{low} and V_{high} are the measured velocities with a low VENC and a high VENC, respectively. The VNR of this method is determined by the lower aliasing velocity only, and should therefore be much higher than a normal, unaliased scan. Also $VENC_{high}$ can be chosen quite high, making the parameter settings less prone to wrongly estimated velocities.

Another method to increase the VNR of in-vivo flow measurements was proposed by Ringgaard [14]. Here a fast scan with low resolution determines the maximum velocity in every heart phase, and the VENC is adapted throughout the cardiac cycle. This method should be less time consuming than the 3-point PC measurement because only two points are acquired. However, a region of interest has to be defined manually in the prescan, requiring more user interaction. All the mentioned methods will be compared later on in Chapter 3.

2.3 Turbulence Quantification

While laminar flow is quite well understood and described by analytical expressions, turbulence exhibits random behavior and so statistical methods are required to model non-laminar flow. In the following the assumption is made that turbulence is an ergodic process which can be described by either averaging over space, time or an ensemble.

2.3.1 Reynolds decomposition and stress tensor

Turbulent flow v_i in an arbitrary direction i can be decomposed into a mean velocity V_i and velocity fluctuations v_i'. [23]

$$v_i = V_i + v_i' \tag{eq. 17}$$

The mean of the fluctuations is zero, but a standard deviation σ_F can be defined:

$$\sigma_{F,i} = \sqrt{\overline{v_i'^2}} \tag{eq. 18}$$

This standard deviation is a measure for turbulence intensity in one direction. To achieve a more general description, using the fluid density ρ the Reynolds stress tensor **R** can be defined as [23]:

$$\boldsymbol{R} = \rho\overline{v_i' v_j'} \sim \rho \begin{pmatrix} \overline{v_1'^2} & \overline{v_1' v_2'} & \overline{v_1' v_3'} \\ \overline{v_2' v_1'} & \overline{v_2'^2} & \overline{v_2' v_3'} \\ \overline{v_3' v_1'} & \overline{v_3' v_2'} & \overline{v_3'^2} \end{pmatrix} \tag{eq. 19}$$

This tensor describes the average momentum flux and its first invariant is directly proportional to the turbulent kinetic energy TKE:

$$TKE = \frac{1}{2}\rho \sum_{i=1}^{3} \overline{v_i'^2} \tag{eq. 20}$$

The unit of turbulent kinetic energy is J/m³. It is a direction-independent measure for the average kinetic energy in a volume due to velocity fluctuations.

2.3.2 Effects of turbulence on the signal

In eq. 12 a homogenous velocity distribution throughout a voxel is assumed. Clearly, in case of turbulent flow or other effects like shear this assumption is not valid any more. If a flow encoding gradient is switched on, dephasing will occur, leading to signal attenuation.

Gao and Gore derived an analytical expression for this decrease in signal magnitude, assuming a Gaussian velocity distribution inside a voxel [12]:

$$S = S_o e^{-\gamma^2 G^2 \sigma_{F,i}^2 T_0 \left[\frac{2}{3}\tau^3 - 2\tau T_0^2 + T_0^3\left(3 - 4e^{-\tau/T_0} + e^{-2\tau/T_0}\right)\right]} \quad \text{(eq. 21)}$$

where τ is the duration of a gradient lobe, and T_0 the characteristic time scale for turbulence, or in other words the time during which a fluid element changes its velocity. Gao and Gore also found solutions for two special cases, one being $\tau \ll T_0$ and the other $T_0 \ll \tau$:

$$\text{for } \tau \ll T_0: \quad S = S_o e^{-1/2\gamma^2 G^2 \sigma_{F,i}^2 \tau^4} \quad \text{(eq. 22)}$$

$$\text{for } \tau \gg T_0: \quad S = S_o e^{-2/3\gamma^2 G^2 \sigma_{F,i}^2 T_0 \tau^3} \quad \text{(eq. 23)}$$

The latter case is an expression similar to the signal attenuation originating from diffusion, using a square bipolar diffusion gradient:

$$S = S_0 e^{-2/3\gamma^2 G^2 D \tau^3} = S_0 e^{-bD} \quad \text{(eq. 24)}$$

Gao and Gore state that T_0 in the ascending human aorta is about 250 ms, and therefore the assumption $\tau \ll T_0$ would be valid. This might be true for steady state flow in a pipe resembling the aorta, but given the oscillatory nature of human blood flow and the fact that flow is not fully developed in that anatomic region, this hypothesis has still to be verified. Given the fact that even with a T_0 of 25 ms (ten times smaller than the estimated value by Gao and Gore) the assumption is still valid, it will be applied in this work.

The different velocities occurring in a voxel can be described using the mean velocity V and the standard deviation of the velocity fluctuations σ_F, which is also called Intravoxel (Spin) Velocity Standard Deviation or *IVSD*. The main focus in all further turbulence considerations lies on this value. Accordingly it will be referred to as σ instead of σ_F hereafter.

Combining eqs. 12 and 22 then gives the final model for a signal depending on k_v:

$$S(k_v) = S_0 e^{-(1/2)\sigma^2 {k_v}^2} e^{i(k_v v + \varphi_0)} \quad \text{(eq. 25)}$$

2.4 Accelerated Imaging

Undersampling of k-space in most cases leads to a degradation of SNR and to aliasing artifacts, depending on the type of undersampling. The main goal of a reduced acquisition of k-space is to shorten acquisition time. In Cartesian sampling the frequency encoding direction is fully sampled, whereas only parts of the phase encodes are acquired.

Many methods have been developed to sample below the Nyquist rate and to repopulate the missing information in the image reconstruction step. For example, information can be gathered from multiple coils to unfold aliased data , either in k-space (e.g. GRAPPA [24]) or in image space (SENSE [25]).

Another undersampling algorithm is k-t-BLAST (Broad-use Linear Acquisition Speed-up Technique) or k-t-SENSE [26]. In most cases when a time series of images is acquired, only limited parts of the field-of-view change and the images exhibit significant correlations in space and time. So it can be said that information is sparse in a suitable linear transform domain and therefore compressible. A recently proposed extension of k-t-BLAST is k-t-PCA, where the training data is subjected to Principal Component Analysis (PCA) to get temporal basis functions to constrain the reconstruction [27].

2.4.1 k-t PCA – Principles

In more detail, the data is undersampled in k_y and t direction (and k_z in the 3D-case), to form a sheared grid. The center of the k-space is sampled fully to obtain a low-resolution training dataset (Fig. 2.4). The larger the training dataset, the smaller the net acceleration factor becomes.

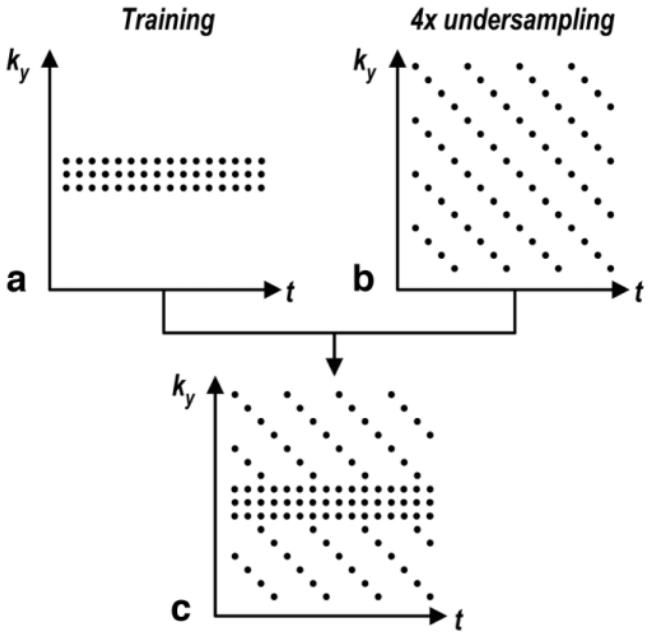

Fig. 2.4: The k-t sampling pattern consist of a training-dataset a) and an undersampled dataset b). Those two sets can be acquired simultaneously (c) [27].

The undersampling leads to an aliasing pattern in x-f space, where every point is a linear combination of the corresponding points of the true object in x-f-space. Instead of trying to reconstruct these points directly, k-t PCA constrains the reconstruction by introducing basis functions (derived from the training images), where every temporal frequency is a linear combination of those basis functions [27] (Fig. 2.5).

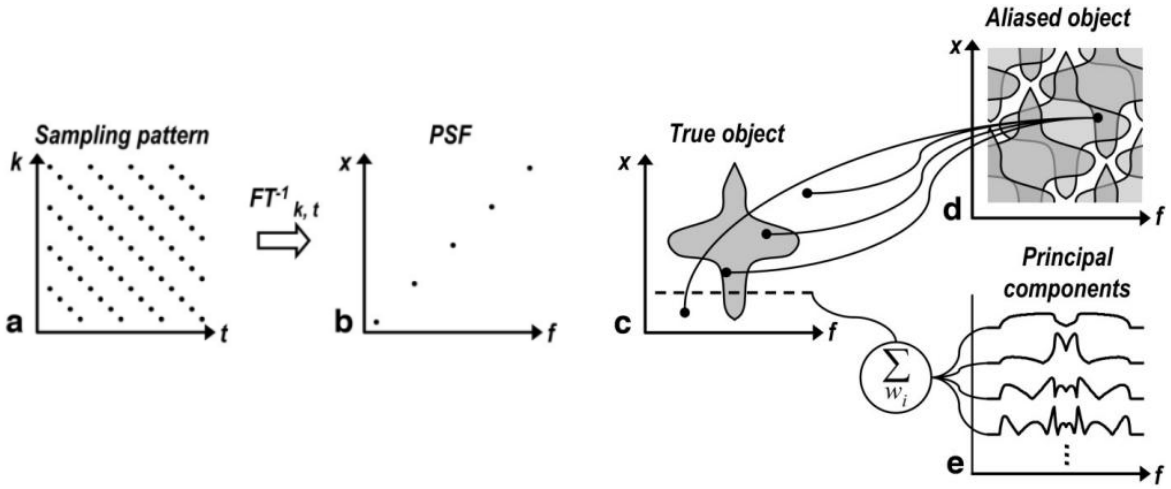

Fig. 2.5: A sheared sampling pattern (a) with an acceleration factor of four leading to a sheared point spread function in x-f space b). Images c) and d) show the true and the aliased object, as well as the composition of a point in the aliased image d). Also shown is an example for the principal components e), of which a linear combination forms a frequency profile of the true object [27].

2.4.2 k-t PCA – Mathematical Formulation

The training data in x-f space is rearranged in a $n_x n_y \times n_f$ matrix $\mathbf{P_{train}}$, where n_x and n_y are the number of pixels in frequency and phase-encoding direction, respectively, and n_f is the number of time frames. This matrix can be decomposed using PCA:

$$\boldsymbol{P_{train}} = \boldsymbol{W_{train}} \boldsymbol{B} \qquad \text{(eq. 26)}$$

The n_{pc} rows of **B** contain the spatially invariant basis functions, and $\mathbf{W_{train}}$ contains the weighting coefficients for the training dataset.

For the true x-f data **P**, a similar combination is assumed:

$$\boldsymbol{P} = \boldsymbol{W}\boldsymbol{B} \qquad \text{(eq. 27)}$$

where the principal components **B** are taken from the training dataset, and **W** has to be found. The aliased data $\mathbf{P_{alias}}$ for a given location x and frequency f_m is given by [27]

$$\boldsymbol{P}_{alias}(x, f_m) = \mathbf{1}\boldsymbol{B_m}\boldsymbol{w_x} \qquad \text{(eq. 28)}$$

where for a 4-fold undersampled dataset **1** = [1 1 1 1],

$$\boldsymbol{B_m} = \begin{bmatrix} \boldsymbol{b}^T(f_{m,1}) & \cdots & 0 \\ \vdots & \ddots & \vdots \\ 0 & \cdots & \boldsymbol{b}^T(f_{m,4}) \end{bmatrix} \qquad \text{(eq. 29)}$$

and

$$\boldsymbol{w}_x = \begin{bmatrix} \boldsymbol{w}^T(x_1) \\ \boldsymbol{w}^T(x_2) \\ \boldsymbol{w}^T(x_3) \\ \boldsymbol{w}^T(x_4) \end{bmatrix} \qquad \text{(eq. 30)}$$

$\mathbf{b}(f_{m,i})$ denotes the $f_{m,i}$-th column of **B** with $f_{m,i}$ being the temporal frequency of the i-th aliasing pixel, and $\mathbf{w}(x_i)$ the row of **W** corresponding to the spatial location of the i-th aliasing pixel.

For every spatial location x the resulting aliased image can be expressed by a combination of all frequencies, giving the signal equation for k-t PCA:

$$\boldsymbol{P}_{alias,x} = \begin{bmatrix} \boldsymbol{P}_{alias}(x, f_1) \\ \boldsymbol{P}_{alias}(x, f_2) \\ \boldsymbol{P}_{alias}(x, f_3) \\ \boldsymbol{P}_{alias}(x, f_4) \end{bmatrix} = \begin{bmatrix} \mathbf{1}\boldsymbol{B}_1 \\ \mathbf{1}\boldsymbol{B}_2 \\ \mathbf{1}\boldsymbol{B}_3 \\ \mathbf{1}\boldsymbol{B}_4 \end{bmatrix} \boldsymbol{w}_x \equiv \boldsymbol{E}\boldsymbol{w}_x \qquad \text{(eq. 31)}$$

This equation can now be solved to obtain $\mathbf{w}_x$, for example using a regularized least squares method. The details of this as well as the calculation of the regularization parameter can be found in [27].

If information about the coil sensitivities is available, it can easily be included in the calculations by replacing the vector **1** in above equations by the sensitivity matrix **S**. This matrix is the same as used for SENSE [25].

As recently suggested [28], reconstruction can be improved by defining spatial compartments in the data, and calculating compartment-specific temporal basis functions. All pixels in such a compartment should show similar dynamic behavior, e.g. in the aorta, and by "tailoring" the basis function to this behavior the reconstruction can be constrained to achieve more accurate results.

2.5 Bayesian Analysis

Conventional phase-contrast methods use two points to encode a single velocity vector component. Using Bayes' theorem, it is possible to incorporate multiple measurements of velocity vector components, and hence it becomes possible to assign a certain probability to each parameter (in this case mean velocity V and the IVSD σ).

2.5.1 Bayesian Parameter Estimation

The basis for the following was taken from a paper by Bretthorst [29], which focused on the Bayes' method for NMR spectroscopy. By maximizing the probabilities for the parameters **θ** one can determine the most probable solution given the measured data M and the model I (eq. 32):

$$P(\boldsymbol{\theta}|M, I) = \frac{P(\boldsymbol{\theta}|I)P(M|\boldsymbol{\theta}, I)}{P(M|I)} \qquad \text{(eq. 32)}$$

The term P($\boldsymbol{\theta}$|I) is the probability of the parameters without any measurements taken, only given the model I. The next term P(M|$\boldsymbol{\theta}$,I) is the probability that a particular set of data was measured, while the parameters and the model are given. This is also called the direct probability of the data [29]. The denominator-term P(M|I) is the marginal probability of the data, given only the model. Because there is no dependence on the parameters, this is just a normalization term and can be left out in the computation.

Following eq. 25, the signal model is defined as

$$S(\boldsymbol{k_v}) = S_0 e^{-(1/2)\sigma^2 k_v^2} e^{i(\boldsymbol{k_v}\cdot\boldsymbol{V}+\varphi)} \quad \text{(eq. 33)}$$

This notation can be split up in a real and an imaginary part s_R and s_I, and assuming additive noise $e(k_v)$ our measured data can be expressed as

$$m_R(k_v) = s_R(k_v) + e(k_v) \quad \text{(eq. 34)}$$

and

$$m_I(k_v) = s_I(k_v) + e(k_v) \quad \text{(eq. 35)}$$

Note that the noise being a function of k_v here only implies that with every measurement a new realization of noise is acquired. Also for simplification only the velocity and ISVD in the direction of the gradient are examined, so this problem becomes 1D. To obtain a full 3D-dataset three orthonormal directions are acquired.

The additional arbitrary phase φ can also be expressed as amplitudes A_1 and A_2, resulting in:

$$s_R(k_v) = [A_1 \cos(V\mathrm{k_v}) + A_2 \sin(Vk_v)] e^{-(1/2)\sigma^2 k_v^2} \quad \text{(eq. 36)}$$

and

$$s_I(k_v) = [A_1 \sin(Vk_v) + A_2 \cos(Vk_v)] e^{-(1/2)\sigma^2 k_v^2} \quad \text{(eq. 37)}$$

Those amplitudes now also have to be expressed using the posterior probability formulation of eq. 32:

$$P(\boldsymbol{\theta}, \boldsymbol{A}|M, I) = \frac{P(\boldsymbol{\theta}, \boldsymbol{A}|I) P(M|\boldsymbol{\theta}, \boldsymbol{A}, I)}{P(M|I)} \quad \text{(eq. 38)}$$

Because the amplitudes A are not exactly known, they can be eliminated by integrating over the probabilities of all possible amplitudes:

$$P(\boldsymbol{\theta}|M,I) = \int P(\boldsymbol{\theta},\boldsymbol{A}|I)P(M|\boldsymbol{\theta},\boldsymbol{A},I)d\boldsymbol{A} \qquad \text{(eq. 39)}$$

But first, the two probability terms have to be evaluated. The direct probability P(M|**θ**,**A**,I) reflects the probability of noise. In this term everything that is known about the noise can be incorporated by choosing a prior. For example, noise carries finite total power. The simplest prior that accommodates this fact is a Gaussian prior:

$$P(\boldsymbol{e}|\sigma_n,I) = (2\pi\sigma_n^2)^{-\left(\frac{N}{2}\right)} e^{-\sum_{i=1}^{N}\frac{e(k_{v,i})^2}{2\sigma_n^2}} \qquad \text{(eq. 40)}$$

where N is the number of (noise) samples **e**. A Gaussian prior does not implicate that the noise is Gaussian as well. However, as long as no additional information regarding the noise is given, it complies with the maximum entropy criterion [29]. The variance of the noise σ_n^2 is assumed to be known for now and will later be eliminated.

Now using eqs. 34 and 35 a direct probability can be assigned to the data M:

$$P(M|s_R,s_I,\sigma_n,I) = (2\pi\sigma_n^2)^{-N} e^{-\sum_{i=1}^{N}\frac{[m_R(k_{v,i})-s_R(k_{v,i})]^2+[m_I(k_{v,i})-s_I(k_{v,i})]^2}{2\sigma_n^2}} \qquad \text{(eq. 41)}$$

The number of samples N here is the number of acquired steps in k_v-space. An assumption made here is that the noise in the real and imaginary part is independent, and therefore $P(M|s_R,s_I,\sigma_n,I) = P(m_R|s_R,\sigma_n,I)P(m_I|s_I,\sigma_n,I)$. Eq. 41 then can be reformulated to be expressed using **A** and **θ**:

$$P(M|\boldsymbol{\theta},\boldsymbol{A},\sigma_n,I) = (2\pi\sigma_n^2)^{-N} e^{-\frac{Q}{2\sigma_n^2}} \qquad \text{(eq. 42)}$$

The expression for Q is rather lengthy, but simply substitutes s_R and s_I in eq. 41 by the expressions in eqs. 36 and 37.

The second term P(**θ**,**A**|I) is independent of any measurements and incorporates given knowledge about the parameters. The chosen prior should not be too rigid and only imposes known bounds such as $-\pi \leq Vk_v \leq \pi$ or $0 \leq \sigma \leq X$, where X is some defined threshold for

the maximum intra-voxel standard deviation to be expected (i.e. 2 m/s or $VENC_{max}$). Within these bounds, a uniform prior is assigned, and eq. 38 can be stated as:

$$P(\boldsymbol{\theta}, \boldsymbol{A}|M, I) \propto \begin{cases} (2\pi\sigma_n^2)^{-N} e^{-\frac{Q}{2\sigma_n^2}} & for\ -\pi \leq Vk_v \leq \pi, 0 \leq \sigma \leq X \\ 0 & else \end{cases} \quad \text{(eq. 43)}$$

In further descriptions, this explicit distinction will not be made and for obvious reasons only the first case will be discussed.

The next step is the elimination of amplitudes **A** through integration according to eq. 39. This can be done analytically through a change of variables. For further information, the interested reader is referred to [29].

The resulting expression reads

$$P(\boldsymbol{\theta}|\sigma_n, M, I) = \sigma_n^{2-2N} \frac{1}{\sqrt{\lambda_1 \lambda_2}} e^{-\frac{\sum_{i=1}^{N}\left[m_R(k_{v,i})^2 + m_I(k_{v,i})^2\right] - 2\overline{h^2}}{2\sigma_n^2}} \quad \text{(eq. 44)}$$

with

$$\lambda_1 = \sum_{i=1}^{N} e^{-\sigma^2 k_{v,i}^2}\left(1 - \sin\left(2vk_{v,i}\right)\right)$$

and (eq. 45)

$$\lambda_2 = \sum_{i=1}^{N} e^{-\sigma^2 k_{v,i}^2}\left(1 + \sin\left(2vk_{v,i}\right)\right)$$

The term $\overline{h^2}$ is the mean square projection of the data onto the model [29], and defined as

$$\overline{h^2} = \frac{1}{2}(h_1^2 + h_2^2) \quad \text{(eq. 46)}$$

with

$$h_1 = \sqrt{\frac{2}{\lambda_1}} \sum_{i=1}^{N} \left[\left(m_R(k_{v,i}) - m_I(k_{v,i})\right) \sin\left(\frac{\pi}{4} - vk_{v,i}\right) e^{-(1/2)\sigma^2 {k_{v,i}}^2}\right]$$

and (eq. 47)

$$h_2 = \sqrt{\frac{2}{\lambda_2}} \sum_{i=1}^{N} \left[\left(m_R(k_{v,i}) + m_I(k_{v,i})\right) \sin\left(\frac{\pi}{4} + vk_{v,i}\right) e^{-(1/2)\sigma^2 {k_{v,i}}^2}\right]$$

As can be seen, in eq. 44 the noise variance σ_n is still assumed to be known, which in most cases is not true. An estimate of the noise variance can be obtained by acquiring noise samples. To eliminate σ_n via integration again a prior is assigned. An uninformative prior for the standard deviation of a Gaussian distribution is the Jeffreys' prior $1/\sigma$ [30].

Multiplying eq. 44 with $1/\sigma_n$ and integrating gives the final result

$$P(\boldsymbol{\theta}|M,I) \propto \frac{1}{\sqrt{\lambda_1\lambda_2}}\left[1-\frac{2\overline{h^2}}{\sum_{i=1}^{N}\left[m_R\left(k_{v,i}\right)^2+m_I\left(k_{v,i}\right)^2\right]}\right]^{1-N} \qquad \text{(eq. 48)}$$

This 2D-posterior probability can now be maximized to find the best estimates for the velocity and ISVD. An example is shown in Fig. 2.6.

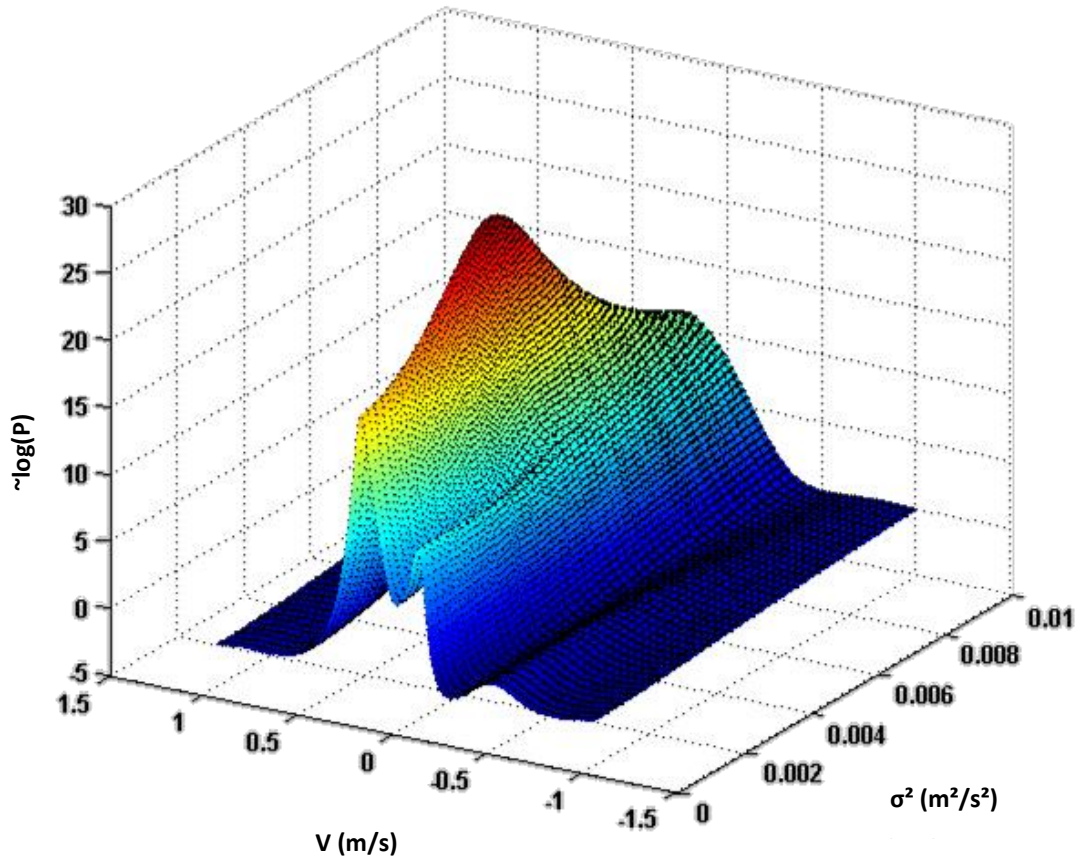

Fig. 2.6: Example of a 2D-posterior probability plot of a noisy data sample (TKE = 6.7 J/m³), with a maximum at V=22 cm/s and σ=6.32 cm/s. Note that a scaling factor for the probabilities is missing, so it is only a relative scale and P>1 becomes possible.

2.5.2 Estimation accuracy

Using Bayes' method, not only the most likely parameters can be found, but also the accuracy of the estimation can be assessed, and a standard deviation given.

Bretthorst derived an expression for the standard deviation for an arbitrary model [29], and adapted to the signal model at hand, the variances of the parameters $\sigma_{\theta 1}^2$ and $\sigma_{\theta 2}^2$ are given by

$$\sigma_{\theta k} = \langle \sigma_n^2 \rangle \left(\frac{u_{1k}^2}{d_1} + \frac{u_{2k}^2}{d_2} \right) \qquad \text{(eq. 49)}$$

with u_{jk} being the k-th component of the j-th eigenvector of the matrix b_{jk}, and d_j being its corresponding eigenvalue. b_{jk} is defined as

$$b_{jk} = -\frac{\partial^2 \overline{h^2}}{\partial \theta_j \partial \theta_k}\bigg|_{\widehat{\boldsymbol{\theta}}} \qquad \text{(eq. 50)}$$

with $\widehat{\boldsymbol{\theta}}$ being the estimation for the parameters. This matrix cannot be evaluated analytically, so numerical methods have to be applied.

The term $\langle \sigma_n^2 \rangle$ in eq. 49 denotes the estimated noise variance, and is simply all measured data which cannot be explained by the model:

$$\langle \sigma_n^2 \rangle = \frac{\sum_{i=1}^{N} \left[m_R\left(k_{v,i}\right)^2 + m_I\left(k_{v,i}\right)^2 \right] - 2\overline{h^2}}{2N - 4} \qquad \text{(eq. 51)}$$

The inclusion of the estimated noise variance in the calculation of the parameter's standard deviation implies that poor data will lead to less accurate measurements as expected.

2.5.3 Including information about the noise

If a noise sample M_n is acquired, this information can also be included in the calculations. The starting point is $P(\boldsymbol{\theta}|\sigma_n,M,I)$ of eq. 44, where the amplitudes have been eliminated and a prior for the noise has to be chosen. If some information about the noise is available, this can be incorporated as well [31]:

$$P(\boldsymbol{\theta}|M_n,M,I) \propto \frac{1}{\sqrt{\lambda_1 \lambda_2}} \int P(\sigma_n|I) P(M_n|\sigma_n,I) P(\boldsymbol{\theta}|\sigma_n,M,I)\, d\sigma_n \qquad \text{(eq. 52)}$$

Here for $P(\sigma_n|I)$, the prior probability of the standard deviation of the noise is again Jeffreys' prior $1/\sigma$. The second term is the direct probability of the noise sample and it was already given in eq. 40. This time it will only be adapted for the measured noise sample $M_n=\{m_{noise,1}, \ldots, m_{noise,Nn}\}$:

$$P(M_n|\sigma_n, I) = (2\pi\sigma_n^2)^{-\left(\frac{N_n}{2}\right)} e^{-\sum_{i=1}^{N_n}\frac{|m_{noise,i}|^2}{2\sigma_n^2}} \qquad \text{(eq. 53)}$$

Evaluating eq. 52 gives [31]

$$P(\boldsymbol{\theta}|M, M_n, I) \propto \frac{1}{\sqrt{\lambda_1\lambda_2}}\left[1 - \frac{2\overline{h^2}}{\sum_{i=1}^{N}\left|m\left(k_{v,i}\right)\right|^2 + \sum_{j=1}^{N_n}\left|m_{noise,j}\right|^2}\right]^{1-N-N_n} \qquad \text{(eq. 54)}$$

Accordingly, the noise samples do not change the probabilities of certain values for the parameters **θ**, but offer a scale against which small effects in the data can be compared to. Also the problem of the term in square brackets (Student-t distribution) becoming singular can be avoided. Apart from the problems of acquiring a meaningful noise sample, the little advantage of such a sample for the given problem of finding the most probable parameters resulted in implementing only eq. 48.

2.6 Measurements and Computation

All scans were acquired on a 3T Philips Achieva System (Philips Healthcare, Best, The Netherlands) with a 6 channel cardiac coil array. The voxel sizes used are mentioned with the corresponding results in chapter 3.

In vivo measurements were performed using ECG-triggering and navigator-based gating with 8-fold acceleration using k-t PCA, leading to scan times of approx. 7-12 minutes (excluding navigator efficiency), depending on the heart rate of the volunteer. Arrhythmia rejection was enabled for all measurements. The maximum VENC was set to 200 cm/s for the volunteers, and 400 cm/s for the patients. Written informed consent was obtained from all volunteers and patients.

All computations and visualization were performed using Matlab (The Mathworks Inc., Natick MA, USA) and GTFlow (GyroTools Ltd, Switzerland).

3 Results

In this chapter the results are presented, at first those based on simulated data, then the in-vitro data using a flow phantom and two models of artificial heart valves and finally in-vivo measurements of both physiological and pathological cases. There is no strict distinction made between results and discussion.

3.1 In-silica

The first part of this work consists of simulated results using a Computational Fluid Dynamics (CFD) dataset of a stenotic U-bend (Fig. 3.1) which provided the 3-dimensional velocity vector field as well as values for the turbulent kinetic energy (TKE).

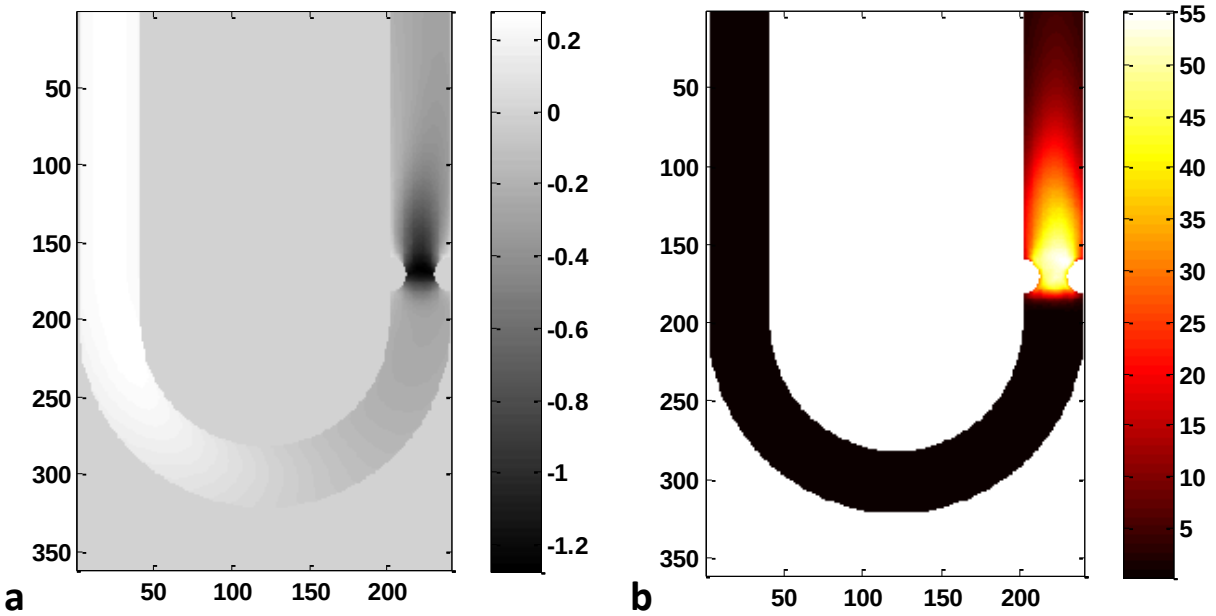

Fig. 3.1: CFD data of a stenotic U-bend, middle slice, a) velocities in y-direction (m/s), b) TKE-values in J/m³.

3.1.1 Velocity encoding

The higher the number of k_v steps used (number of segments), the more information is available for the Bayesian parameter estimation, and the VNR increases. But with every additional segment the scan time increases as well and accordingly the maximum number is

limited due to practical considerations. A reasonable number of velocity encodings proved to be three steps in every direction. Consequently a total of 10 segments (3*3 + 1 reference segment) are acquired with a scan time of around 8 min excluding navigator efficiency.

There is one condition for the choice of k_v values: one of the segments in each direction has to have a low k_v value, meaning that the corresponding VENC is higher than any occurring velocity to avoid phase wraps. If this condition is met, the other encoding strengths can be chosen in a way that the VENC is lower than V_{max} – which is recommendable to achieve a high VNR – and the resulting phase wraps will be resolved by the algorithm.

To test how to choose the remaining k_v steps, the CFD data was run using different combinations of segments. The results can be found in Table 3.1.

	TKE		**$\lvert V_{xyz} \rvert$**	
Gradient First Moment	**RMSE (cm/s)**	**Median Error in %**	**RMSE (cm/s)**	**Median Error in %**
SNR 15				
1, 2	22,51	91,25	3,19	7,52
1, 6	3,93	13,20	1,29	2,89
1, 8	15,36	11,33	1,37	2,18
1, 3, 5	4,08	16,64	1,51	3,56
1, 3, 7	3,30	11,31	1,19	2,60
1, 4, 8	**3,01**	9,92	1,04	2,25
1, 7, 8	7,00	**8,35**	**1,01**	**1,90**
1, 3, 5, 8	2,65	9,24	1,02	2,26
1, 2, 4, 6, 8	2,34	8,18	0,99	2,17
1-8	1,89	6,84	0,93	2,04
SNR 10				
1, 3, 5	6,11	24,26	2,25	5,32
1, 4, 8	**4,67**	15,06	**1,59**	3,41
1, 7, 8	14,62	**13,22**	1,91	**2,85**
SNR 5				
1, 6	47,68	41,61	19,27	10,06
1, 3, 5	**19,85**	50,46	**4,59**	10,54
1, 4, 8	27,59	**33,10**	11,35	**6,97**

Table 3.1: Comparison of calculation accuracy using a selection of different gradient first moments at different noise levels. A gradient strength of i equals VENC = 200/i cm/s, RMS_{TKE} was 24.3 J/m³, RMS_{Vall} = 31.96 cm/s. The best values for each combination of 3 segments are written in bold.

One error metric used was the root mean square error RMSE, which is defined as

$$RMSE = \sqrt{\frac{\sum_{i=1}^{n}\left(x_{calc,i} - x_{act,i}\right)^2}{n}} \qquad \text{(eq. 1)}$$

where n is the number of pixel, and x_{calc} and x_{act} are calculated and true values, respectively. The values alone are not very meaningful except for relative comparison, although they can be set in relation to the RMS value of the considered area to get an RMSE in percent.

The other metric used was the median percentage error, which is computed by expressing the error as a percentage for every pixel, and then taking the median. The median was used, because in pixels with very low values the error in percent is very large and would distort the result. For the TKE calculations, only the post-stenotic part of the U-bend was considered.

3.1.2 Accuracy at different noise levels

Another point to consider is the behavior of the algorithm at different noise levels. Here a combination of three encoding segments per direction was used, with VENCs of 200, 50 and 25 cm/s (so gradient first moments of 1, 4 and 8 using the notation of Table 3.1).

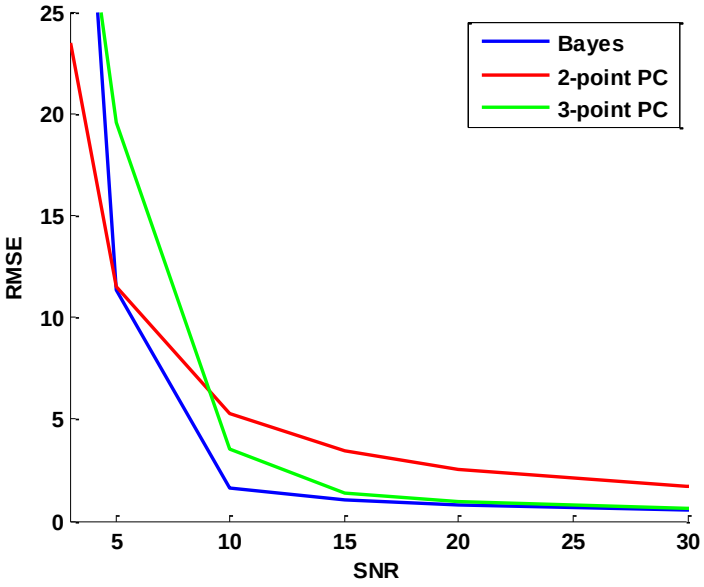

Fig. 3.2: Root Mean Square Error (RMSE) of different techniques to compute the velocity amplitude $|V_{xyz}|$.

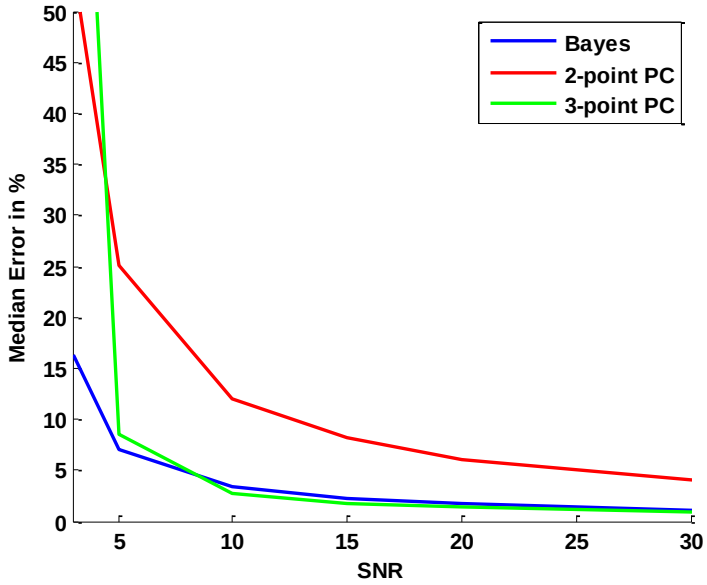

Fig. 3.3: Median error in % of different techniques to compute the velocity amplitude $|V_{xyz}|$.

An SNR regime of 1 to 50 was considered, and the results can be found in Fig. 3.2 and Fig. 3.3. The results from the Bayesian technique were also compared to standard 2-point phase contrast measurements as well as to the 3-point technique described by Lee et al [15]. To compensate for the different scan times, the 2-point results were divided by $\sqrt{3}$ and the 3-point data by $\sqrt{1.5}$, assuming that N averages result in a $\sqrt{N}$ reduction of noise.

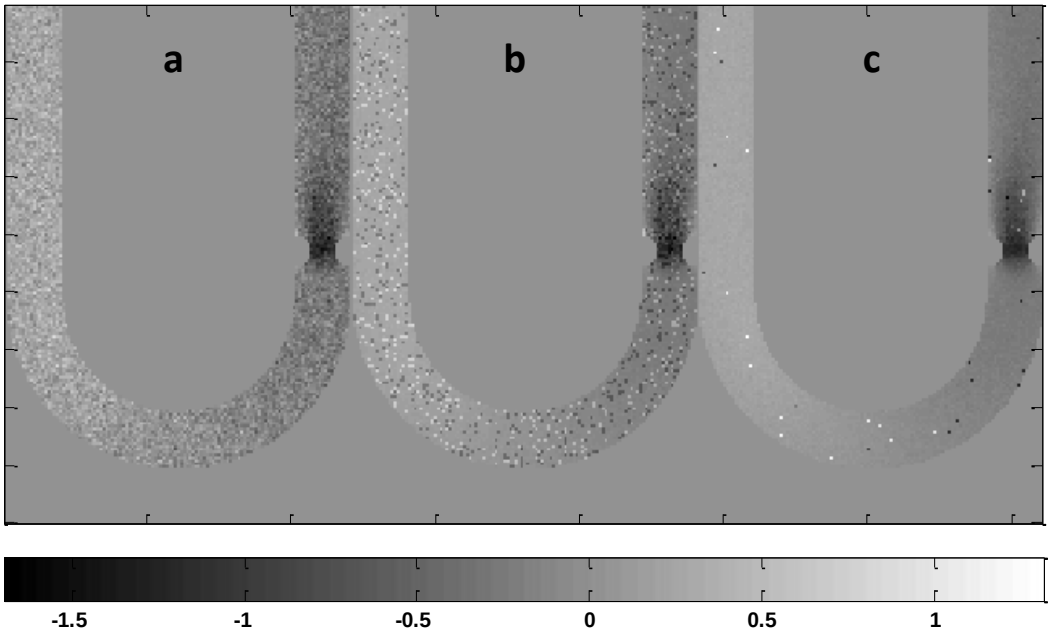

Fig. 3.4: Comparison of velocities V_y (in m/s) using a) conventional 2-point PC measurement, b) 3-point PC, and c) Bayesian Analysis. SNR 5, voxel size 1 mm isotropic. The 2- and 3-point measurements are taken without any averages, so they would have a shorter scan time than the 4-point Bayes calculation (factors 2 and 1.5, respectively).

3.1.3 Pulsatile Flow

The performance of the algorithm proposed cannot be fully analyzed using static flow. During a heartbeat, a wide range of velocities occur and the method should provide accurate results in any flow condition. To simulate pulsatile flow, a waveform similar to the actual conditions in the ascending aorta was applied to the CFD data.

The Bayesian approach was again compared to the 3-point PC measurement, and also to a technique proposed by Ringgaard [14] (see chapter 2), which is a conventional 2-point PC measurement with varying VENC throughout the heart cycle. In Fig. 3.5 a comparison of the methods can be seen, where an average of the velocities within a ROI was taken. The SNR was set to 10, and shorter scans like the 2-point PC were averaged to achieve comparable scan times.

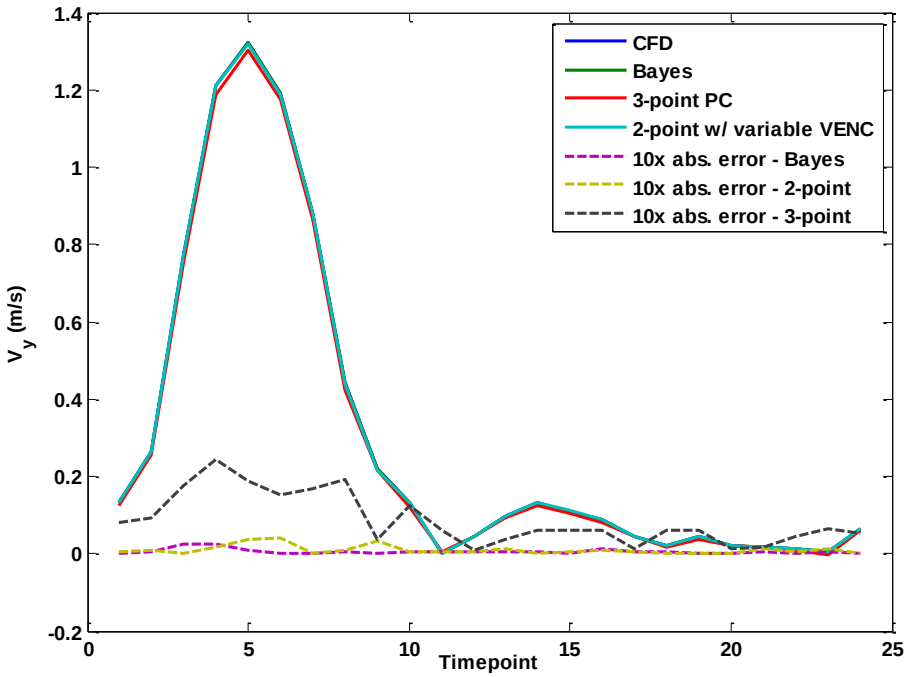

Fig. 3.5: Comparison of the averaged velocities throughout a heart cycle, measured using different techniques.

All the methods showed a good correlation with the original CFD data, except for the 3-point PC which underestimated the velocities to some extent.

To get a better picture of the accuracy of the different techniques, the VNR was calculated for every time point and the results can be found in Fig. 3.6. Again, the Bayes approach performed best, but the 2-point PC method with variable VENC showed higher VNR than the 3-point method.

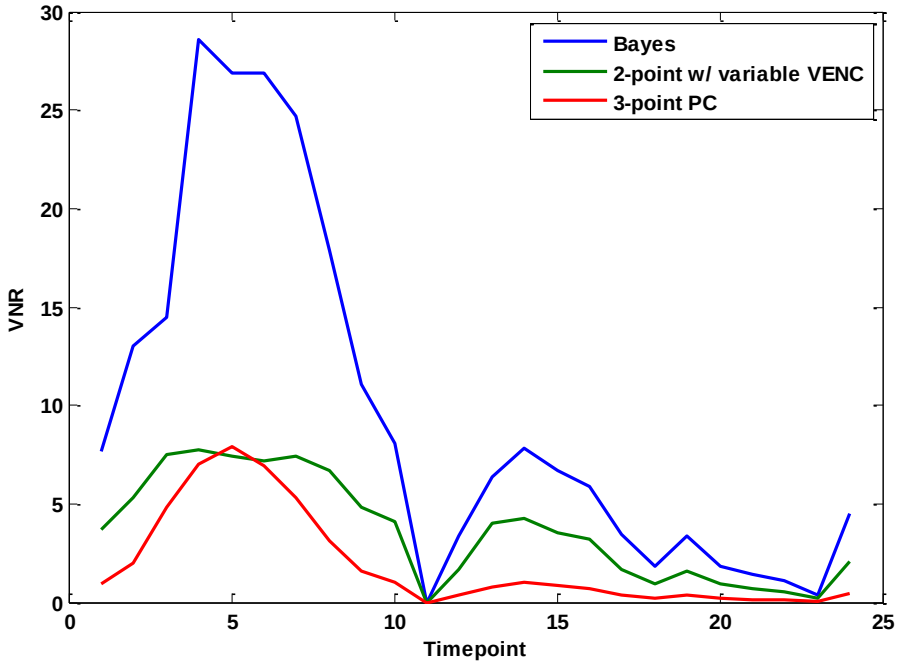

Fig. 3.6: VNR of different velocity reconstruction techniques during the heart cycle.

3.1.4 Discussion of the in-silica results

As can be seen in Table 3.1, the accuracy of the calculation does not depend much on the individual gradient first moments as long as k_v space is covered uniformly. If all steps are clustered, the error increases. If only two segments per direction are used it is advisable to set the first to a non-aliasing VENC, and the other one to a VENC about 1/4 to 1/6 of the higher encoding velocity, depending on the expected SNR.

In general it can be said that very high first moments do not contribute to a higher accuracy, especially if turbulence is present. This is related to signal loss due to dephasing at high first moments. Simulations with low SNR show that this effect becomes more prominent with a higher noise level. The median error will be reduced, but the mean squared error is increased. Consequently, there will be a few pixels where the computed velocity deviates significantly from the CFD data.

The SNR regime of 5-15 corresponds to values expected for typical in-vivo measurements depending on the acceleration factor used. As can be seen in chapter 3.1.2, this corresponds to noise levels where the probabilistic approach starts to outperform the 3-point PC approach. At higher SNR the fact that only the highest first moment is considered proves to be a slight advantage, so the median error (Fig. 3.3) is lower with 3-point PC. In terms of

RMSE (Fig. 3.2) the Bayesian analysis performs better at all SNRs. The conventional 2-point PC measurement cannot compete with the other two methods at any reasonable SNR, but it has a lower error at a very low signal-to-noise ratio of 3. This is also the breakpoint for the multi-point methods. The large difference between median and mean values can be explained by looking at the computed velocities more closely. If the noise is too high, correct unwrapping is no longer possible in some pixels, which leads to large deviations in these points. This manifests in salt-and-pepper noise (Fig. 3.4).

It should also be pointed out that the k_v values were chosen to perform well with all SNRs. If the SNR is approximately known beforehand, a smaller error can be achieved. For example, using VENCs 200, 28.5 and 25 (1, 7, 8) in combination with an SNR of 30 or better, also the median error is lower than using 3-point PC measurements.

The erroneous results at an SNR of 3 can be addressed by increasing the number of k_v steps. This is comparable to an increase in SNR by averaging, although different k_v points should provide additional information leading to more accurate results. Using 5 k_v steps at SNR 3 results in an RMSE of 14.5 cm/s, and a median error of 11.5%.

The results of the pulsatile waveform differ slightly from the static approach. Fig. 3.5 shows a very good agreement between all the results despite the low SNR. But this is misleading – assuming Gaussian noise, the errors would cancel out. The underestimation of the 3-point approach can be explained by the salt-and-pepper noise described earlier. The same noise also strongly influences the standard deviation of the velocity error, leading to a very poor VNR throughout the heart cycle. This also shows that simple averaging of two 3-point PC scans would not lead to a drastic improvement, because of the spike-like appearance of falsely resolved phase wraps.

Fig. 3.5 is also a good example for the difficulties, which can arise from using VNR as a quality measure. To compare individual methods, data with similar mean velocities have to be used, and as the mean velocity approaches zero like at time point 11, VNR differences become too small to be resolved accurately.

3.2 In-vitro

This chapter shows the feasibility of the presented technique to assess different flow scenarios. Two different artificial heart valves are investigated and results regarding image degradation using accelerated imaging are presented.

3.2.1 Artificial Heart Valves

The two devices investigated were a Saint Jude Medical (SJM) mechanical aortic valve (Saint Jude Medical, Saint Paul, MN), and an Edwards Sapien transcatheter heart valve (Edwards Lifesciences Corporation, Irvine, CA) which is a ballon-expandable, trifleaflet bovine valve (Fig. 3.7). It is implanted using a catheter to access the stenotic aortic valve through one of the larger arteries, a procedure termed “Transcatheter Aortic Valve Implantation” (TAVI). Both devices were placed in the same custom build flow phantom providing pulsatile flow.

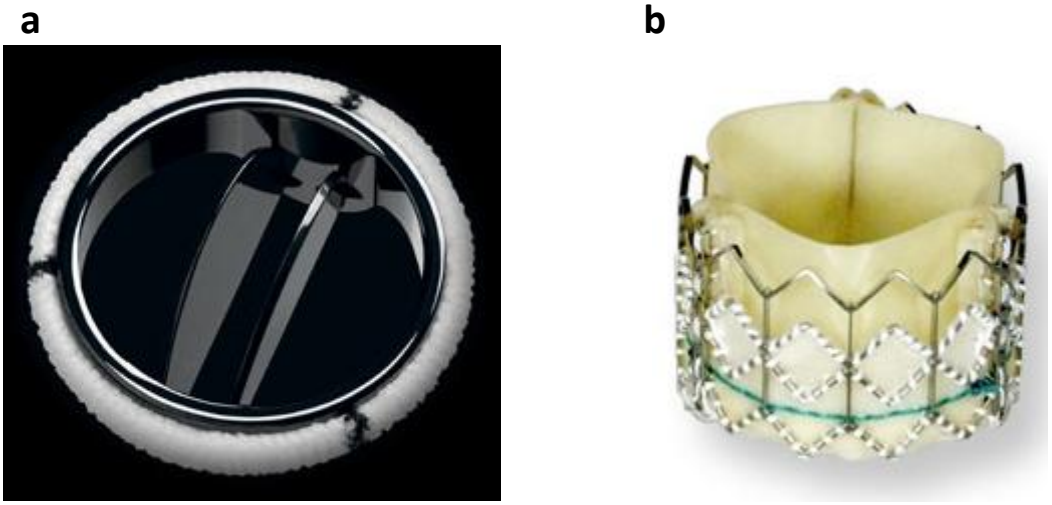

Fig. 3.7: Images of a) the Saint Jude Medical aortic valve and b) the Edwards Sapien transcatheter heart valve (images courtesy of www.sjm.com and www.edwards.com).

An overview of the flow conditions during peak flow can be seen in Fig. 3.8, and a more detailed map of turbulence and velocities in slices in the direction of flow can be found in Fig. 3.9 and Fig. 3.10 for the Edwards valve and the SJM mechanical valve, respectively. Fig. 3.11 shows the middle slice along the phantom during peak flow.

The data was acquired without undersampling and eight steps in k_v space were used in each direction to achieve maximum accuracy.

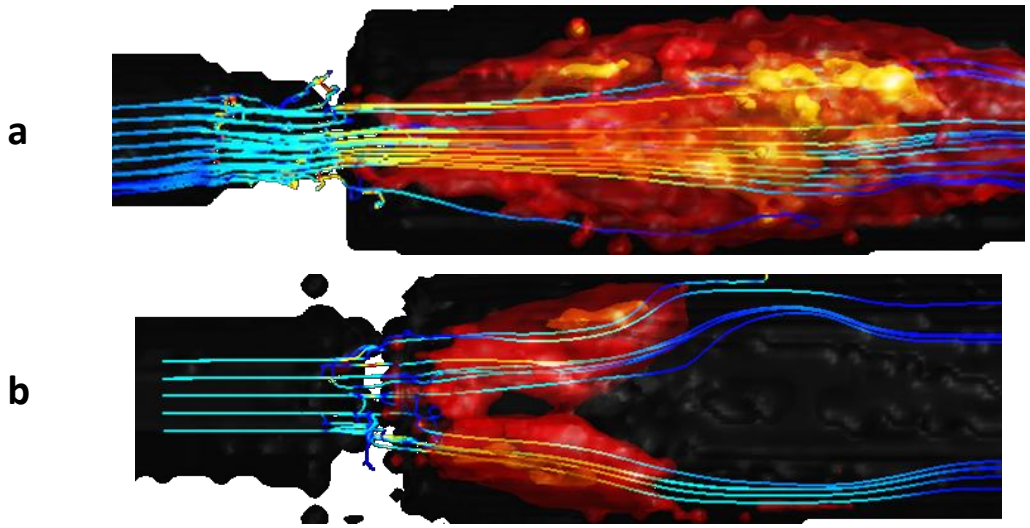

Fig. 3.8: Isosurface rendering of TKE and streamlines in the Edwards valve (a) and the SJM valve (b). The values of the isosurfaces were set to 50 J/m³ (red), 100 J/m³ (orange) and 125 J/m³ (yellow).

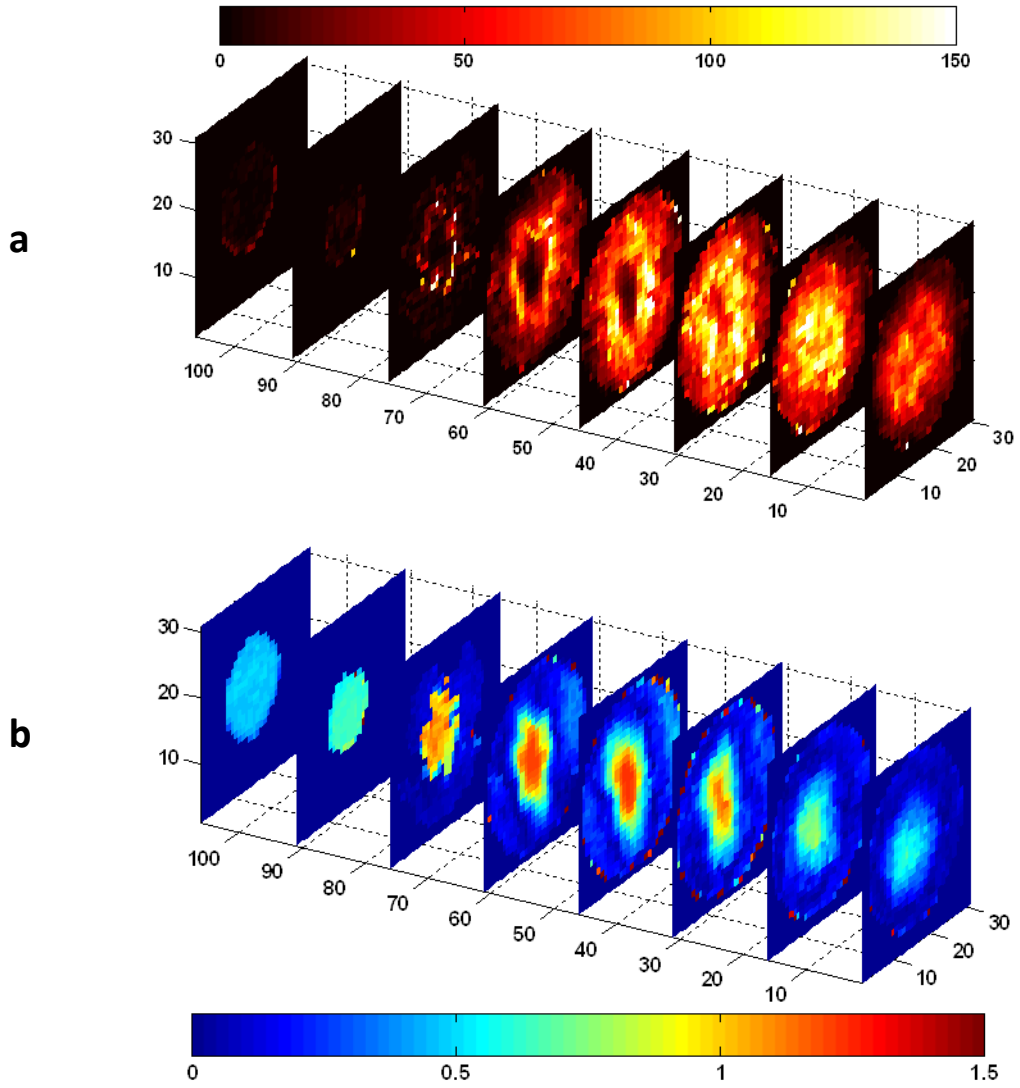

Fig. 3.9: Turbulence in J/m³ (a) and velocities in m/s (b) for the Edwards valve during peak flow. The valve is located approximately at position x = 80, and flow is directed in negative x-direction.

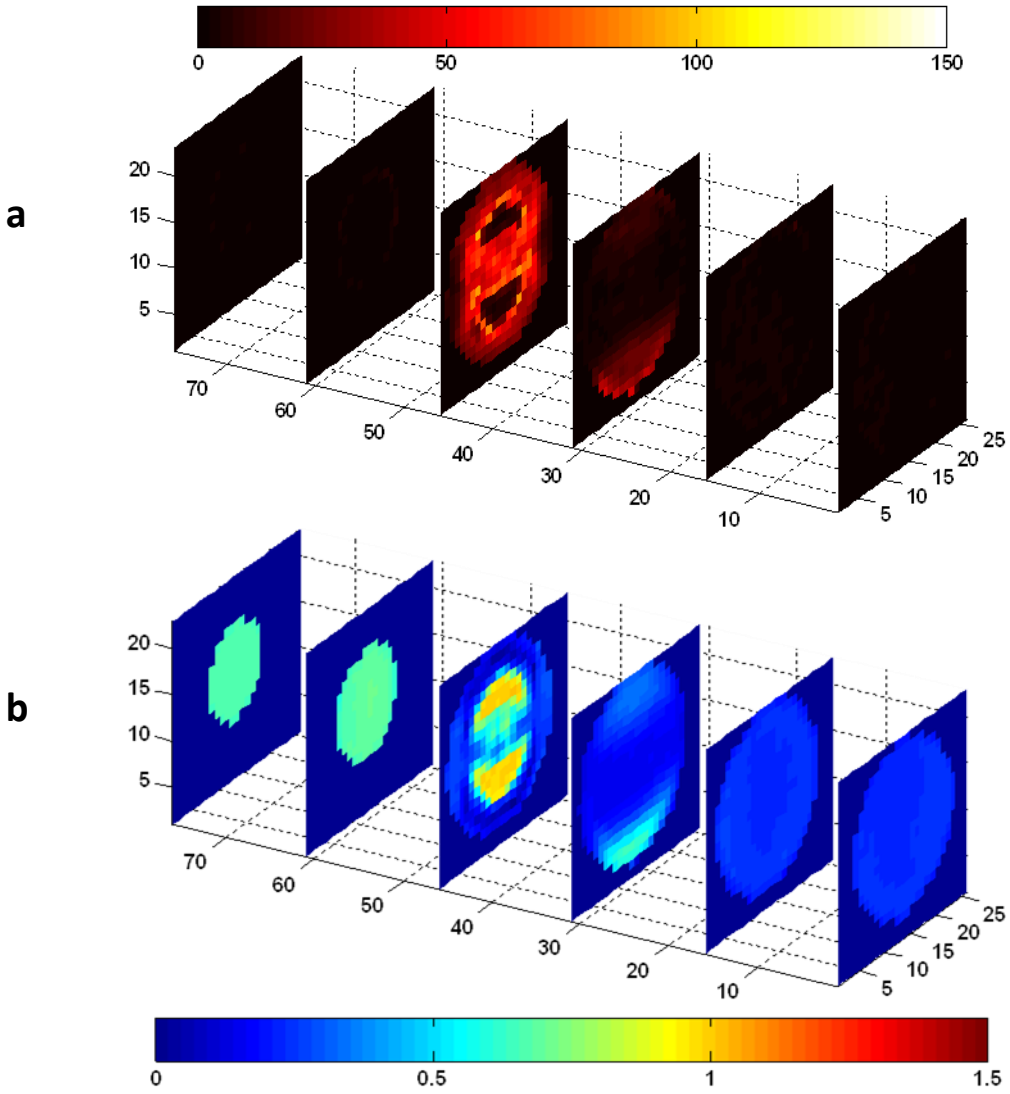

Fig. 3.10: Turbulence in J/m³ (a) and velocities in m/s (b) for the SJM mechanical valve during peak flow. The valve is located approximately at position x = 55, and flow is directed in negative x-direction.

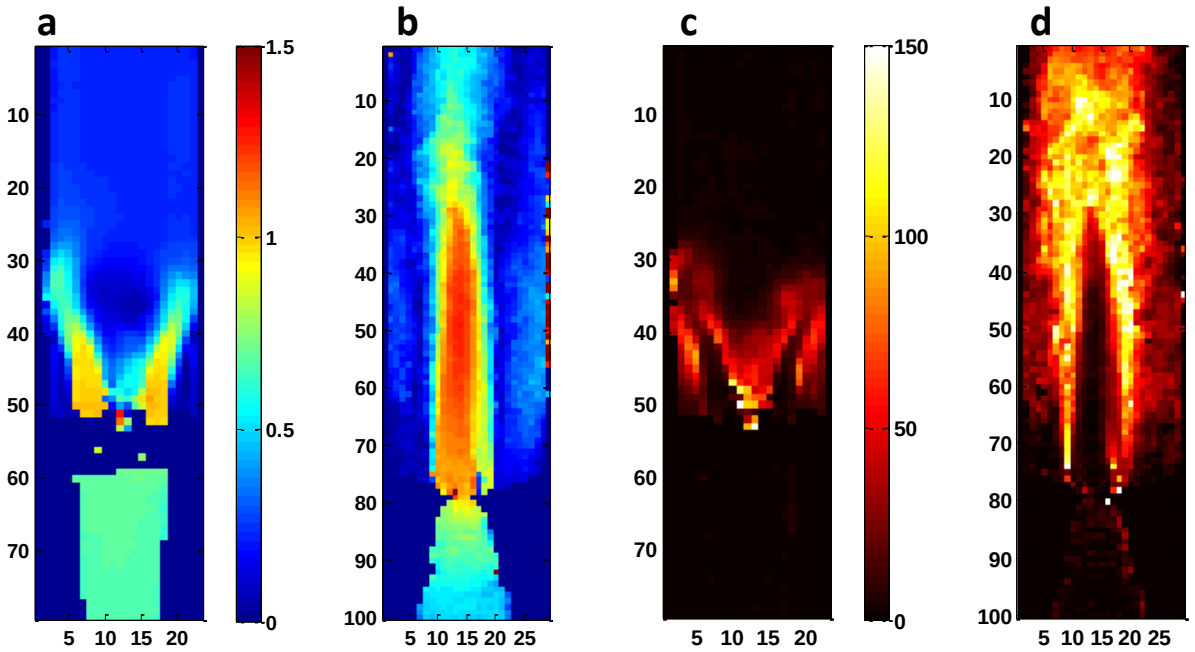

Fig. 3.11: Velocity and turbulence profile along the flow axis of the SJM bileaflet valve (a, c) and the Edwards trileaflet valve (b, d). Units are m/s and J/m³. Please note the different scaling of images **a**, **c** vs. **b** and **d**.

3.2.2 k-t PCA

To assess the effects of undersampling on measurement accuracy, different acceleration factors were employed and the results compared. The flow conditions using the SJM mechanical valve were fully sampled as a reference, using eight k_v steps in every direction. For the reconstruction of the different acceleration factors three steps were used. In addition, for the 16-fold undersampled measurement (termed kt16 from now on) a reconstruction employing 5 segments was performed.

In Fig. 3.12 the velocities throughout the simulated heart cycle in a single voxel can be seen. It was located 1.5 cm upstream of the center of the valve. There is retrograde flow starting at time point 20, leading to a closure of the valves at time point 22. The sharp peak at the end results from the formation of a jet, when the fluid is pressed through the gap between the leaflets. If the mean of that area were taken, the correspondence between the curves would have been even better.

It was previously reported (i.e. [32]) that k-t BLAST and k-t SENSE lead to an underestimation of peak velocities because of temporal low-pass effects. These findings could not be replicated using k-t PCA.

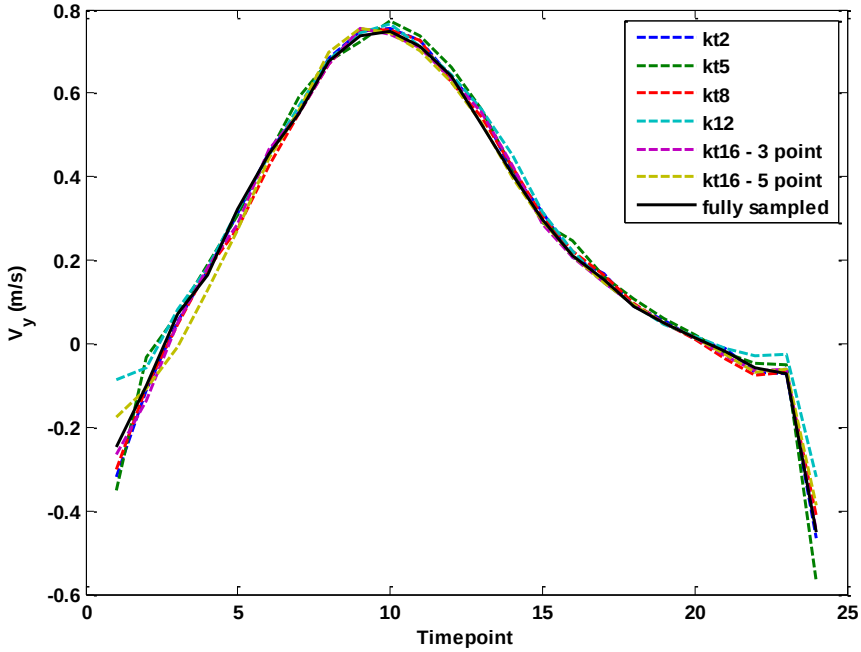

Fig. 3.12: Time course of the velocity in one voxel, located 1.5 cm upstream of the valve center. Jet formation during retrograde flow can be seen at time point 24.

The VNR throughout the heart cycle (Fig. 3.13) in a region with mostly laminar flow is comparable between undersampling factor of 8 (kt8), using three points in k_v-space and 16 (kt16) with five points. There is a decrease in VNR using the same amount of k_v steps and for higher acceleration factors, as expected.

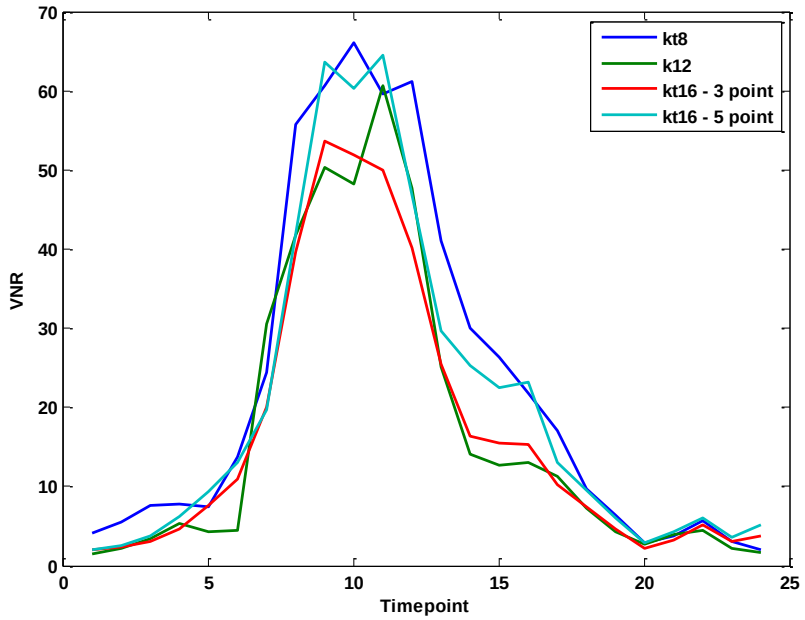

Fig. 3.13: VNR in a ROI in front of the valve, where flow is mostly laminar. Different acceleration factors are compared for every time step.

For the turbulent flow downstream of the valve the VNR is diminished by a factor of approximately 4. In Fig. 3.14 the root mean square error (RMSE) in that volume is displayed. The relative error is the largest when high turbulence is present (time points 9-10), partly resulting from decrease in signal magnitude and therefore higher phase errors at high k_v values.

The relative error for the TKE is about two times the RMSE for the velocities.

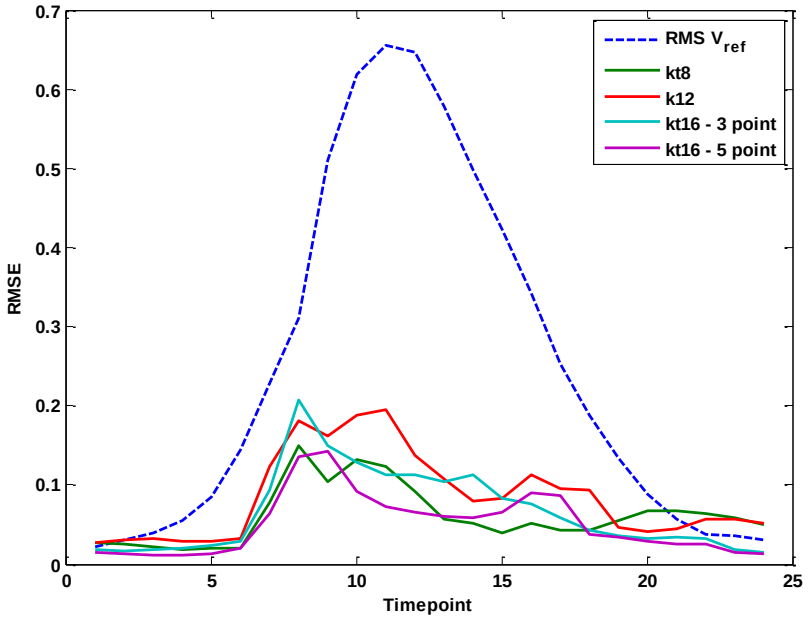

Fig. 3.14: Root Mean Square Error of the measured velocities for different acceleration factors in a volume downstream of the valve. The reference RMS value for the volume is also displayed (dotted line).

3.2.3 Discussion of the in-vitro results

The comparison of the two artificial aortic valves clearly shows differences in the flow patterns downstream of the valve. In the isosurface renderings (Fig. 3.8) only the Edwards Sapiens valve shows TKE values above 100 J/m³, and also in the subsequent images higher peak velocities and turbulence values are observed.

Turbulence mostly occurs where the jet breaks down. Accordingly, the more abrupt the transition between areas of high and low velocities the higher the TKE. Given that the trileaflet valve emits only one jet with small diameter, whereas the bileaflet mechanical valve forms two broader jets, the results seem plausible. Also Kvitting et al [33] found similar relations of mechanical and xenographic valves. Because of the changes in flow direction

downstream of the mechanical valve – the flow is directed towards the vessel walls – the behavior in-vivo can be different. It is possible that the curvature of the aorta can lead to one jet being directed towards the vessel wall, leading to abnormal wall shear stresses.

Another point in the assessment of artificial heart valves is the amount of regurgitation. Because of insufficient closing, blood is able to leak from the aorta into the heart, leading to a decreased efficiency of every heartbeat. Both valves showed some degree of regurgitation, but because of signal loss the exact amount was not quantifiable. However, higher amounts of turbulence during retrograde flow of the SJM mechanical valve could be observed, most probably resulting from small gaps between the leaflets.

For laminar flow, the accelerated acquisition barely affects the accuracy of the measurements. Also no underestimation of peak flow velocity was detected using k-t PCA. The deviations at time point 1 in Fig. 3.12 are possibly a result of the reconstruction of the undersampled images, because the framework pads the image dimensions during processing, which can lead to errors at the first and last time point.

The time course of the flow also illustrates one major drawback of prospective triggering – the last part of the cardiac cycle is not imaged, making it impossible to determine how long the diastolic retrograde flow actually lasts. In this case, most of the cycle should have been imaged, because of the fixed heart rate of the phantom the percentage measured could be maximized.

Fig. 3.13 and Fig. 3.14 indicate that image quality decrease at higher acceleration factors is still acceptable, and that the lower SNR can be compensated by acquiring additional points in k_v-space. The ideal choice depends on the main focus of the measurement. If more points are acquired at a higher acceleration factor, the accuracy of the TKE results increases, but the salt-and-pepper noise in velocity measurements increases as well. The factors stated here are nominal values, the effective values depend on the amount of training data acquired. Nominal 8-fold undersampling (kt8) leads to an effective acceleration of 6.6, and kt16 results in 11.3-fold acceleration. In vivo these values would be higher, because of the form of the phantom the number of points acquired in phase encoding direction is lower than in typical in-vivo scans. In terms of total scan time, the 16-fold undersampled measurements with 5 points in k_v-space could be acquired quicker than using 8-fold undersampling, but would still lead to more accurate results.

3.3 In-vivo

For the in-vivo data six healthy volunteers and two patients were scanned. Patient 1 had a severe aortic valve stenosis, patient 2 had a TAVI valve implanted two years before the scan. Two scans were performed, including the left ventricular outflow tract (LVOT) and the aortic arch.

3.3.1 Physiological cases

In the healthy volunteers flow was generally laminar with only little turbulence measured. The peak TKE values during the heart cycle were around 80-250 J/m³ depending on the volunteer. Example images of the left ventricular outflow tract (LVOT) during the ejection phase and the filling phase can be seen in Fig. 3.15. The vertical view of the LVOT of another volunteer can be found in Fig. 3.16, but only for the ejection phase as this view does not depict the filling of the left ventricle. Note that the underlying magnitude images result from the same scan making it possible to estimate SNR.

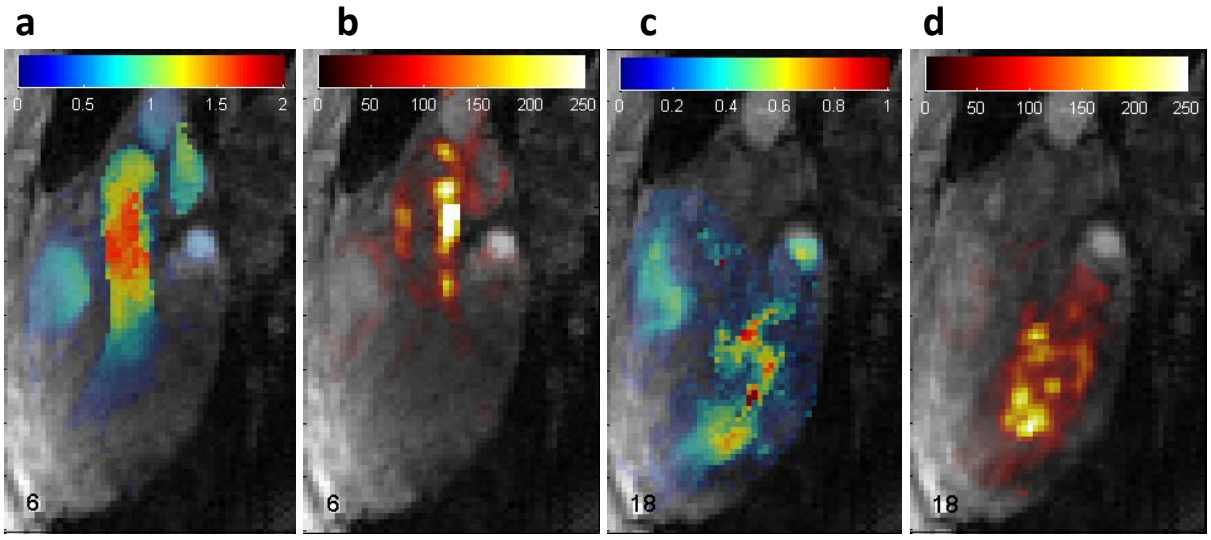

Fig. 3.15: Velocities and TKE in the LVOT of a healthy volunteer during the ejection phase (a, b) and during the filling phase (c, d) of the heart. Units are in m/s for the velocities and J/m³ for TKE.

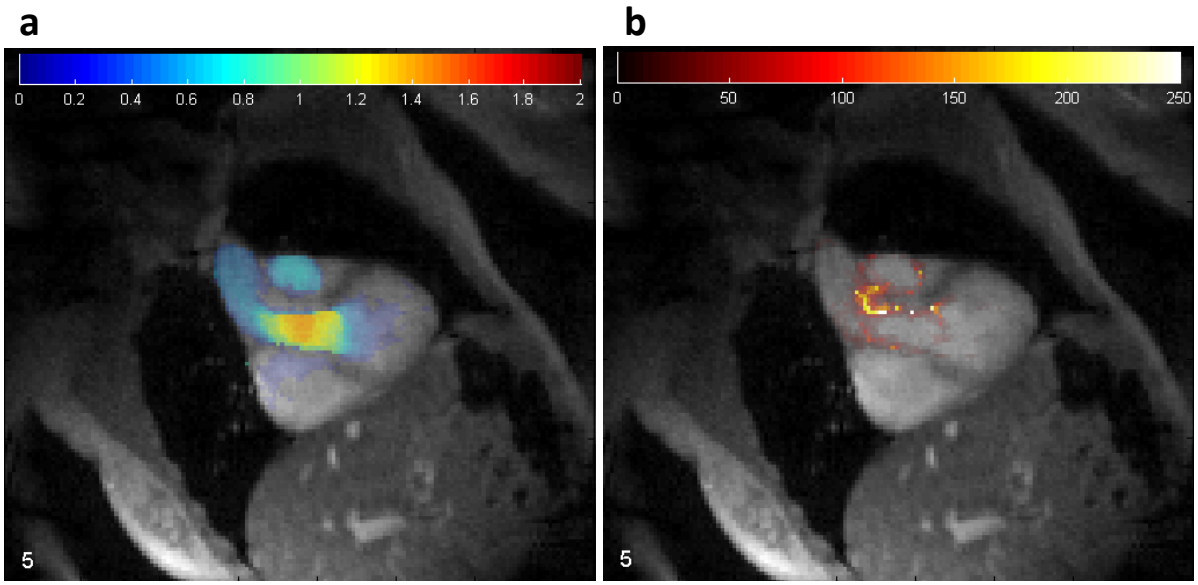

Fig. 3.16: The vertical LVOT of another healthy volunteer during systole, again depicting velocities (a) and turbulence (b). Possible shear at the vessel walls is interpreted as turbulence by the algorithm.

3.3.2 Pathological cases

Two pathological cases were studied in this work, patient 1 suffered from severe stenosis of the aortic valve, and patient 2 had a TAVI valve implanted two years prior to the scan. The valve used was not the Edwards Sapien valve tested in-vitro, but a similar trileaflet xenovalve (*Medtronic CoreValve,* Medtronic Inc., Minneapolis, MN).

In Fig. 3.17 the left ventricular outflow tract (LVOT) of patient 1 is shown during the ejection phase, and the TKE and velocities are plotted. Fig. 3.18 shows a similar view for patient 2 (slightly different angle) where the position of the valve is being clearly visible because of signal loss.

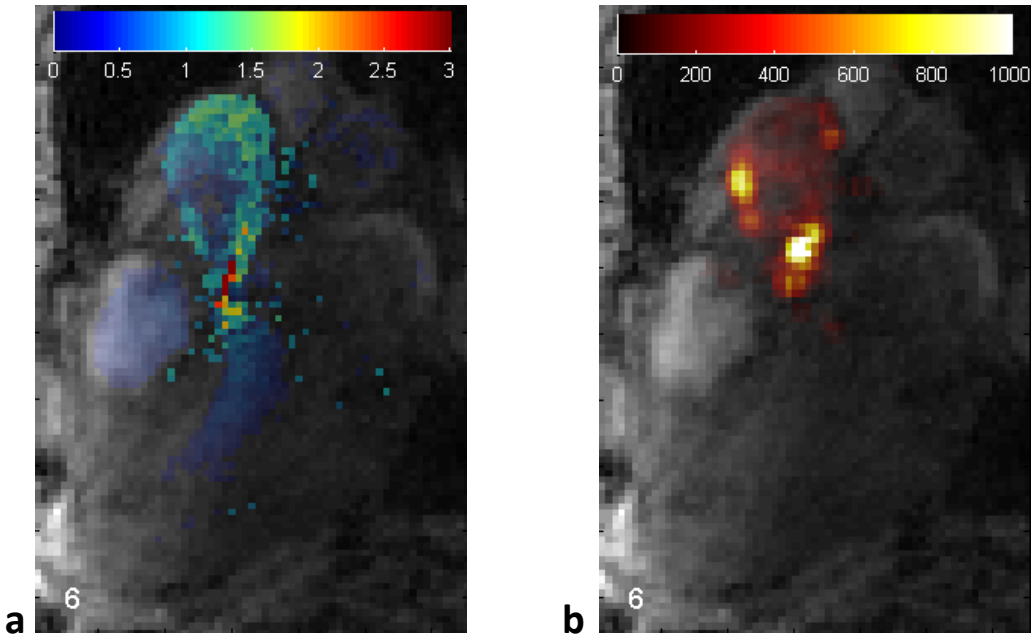

Fig. 3.17: Velocities (a) and TKE (b) in a patient with a stenotic aortic valve. Only a small part of the aorta lies in the imaged plane. The jet is directed towards the vessel wall.

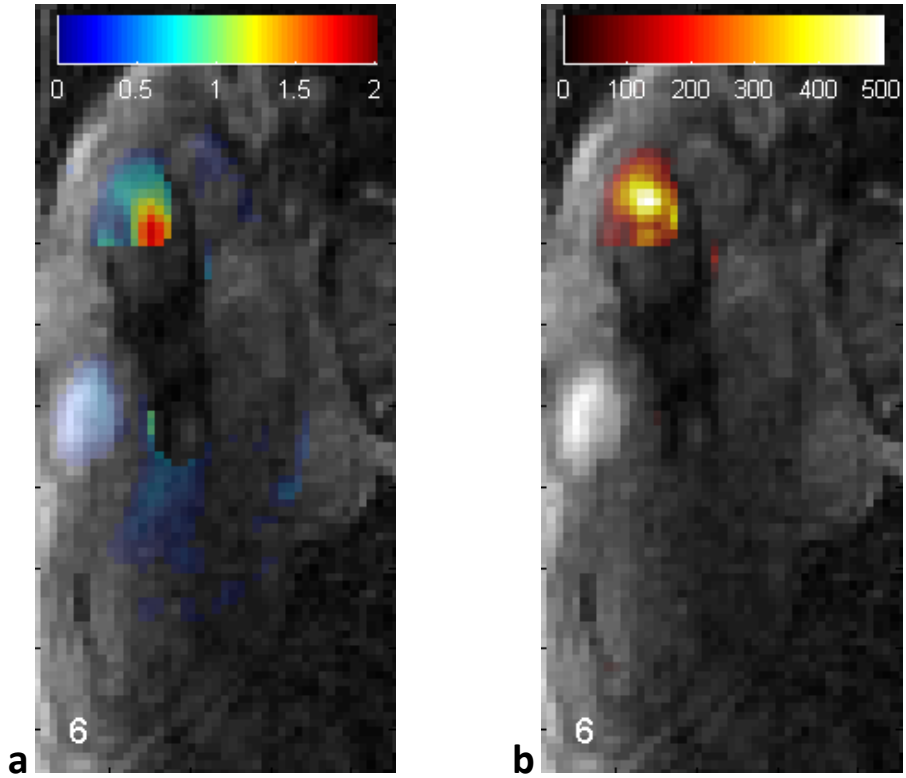

Fig. 3.18: LVOT of a patient with TAVI valve. The valve is clearly visible because of signal loss, and the results from that area were masked. The jet visible does not end abruptly but exits the plane.

To get a better picture of the flow patterns in the aorta, isosurface renderings of the aortic arch were prepared and can be found in Fig. 3.19 for patient 1, Fig. 3.20 for patient 2 with the TAVI valve and for a healthy volunteer in Fig. 3.21. Isovalues were set at 262.5, 500 and 1000 J/m³. The streamlines also show helical flow in both patients.

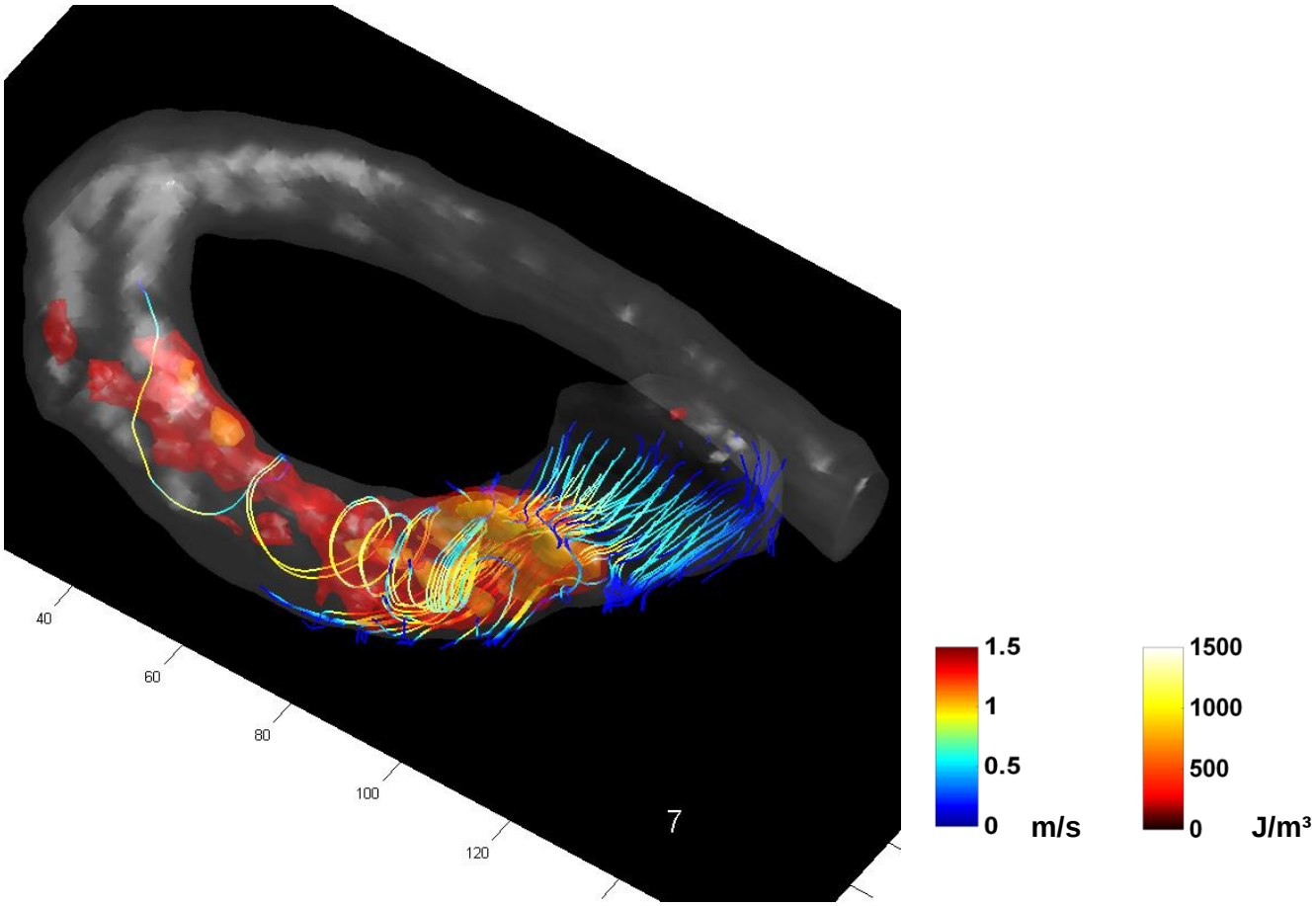

Fig. 3.19: Isosurface rendering of the aortic arch of a patient with stenotic aortic valve.

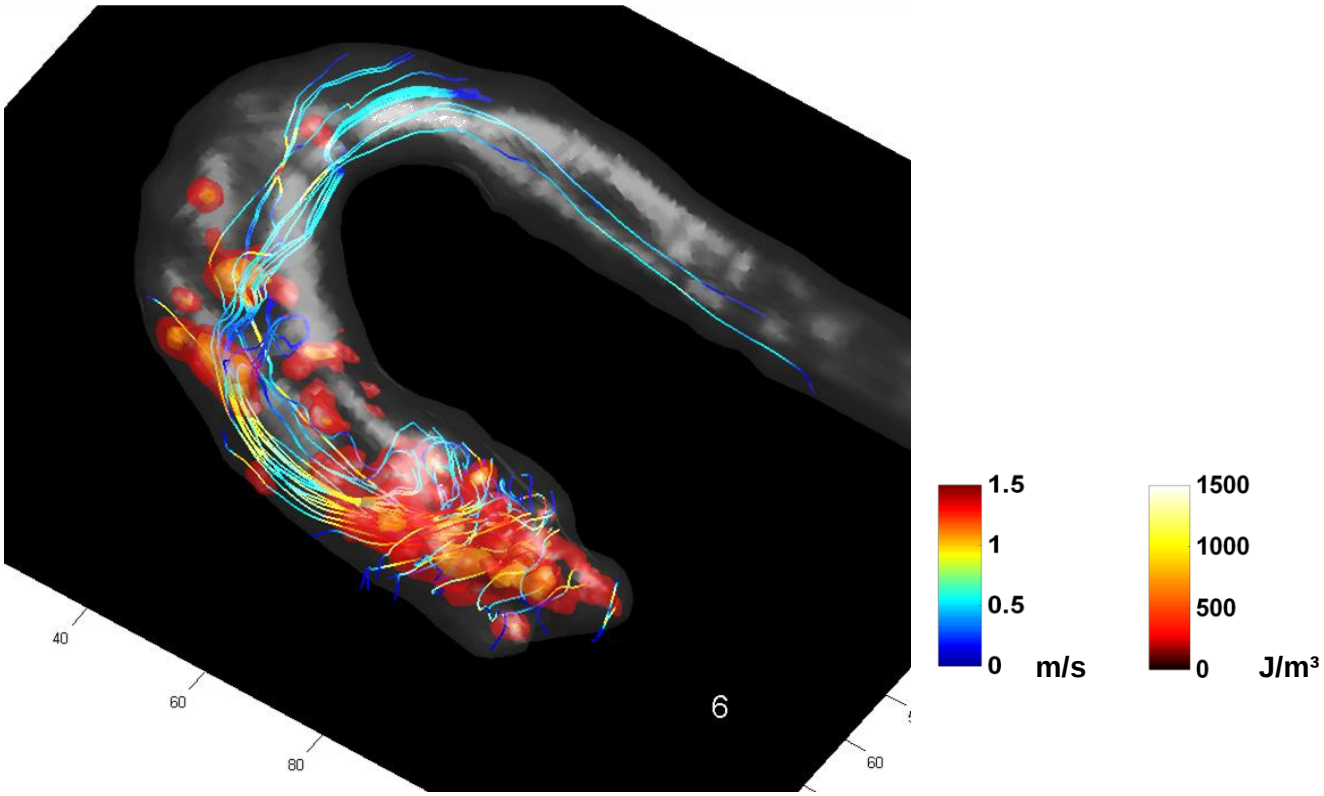

Fig. 3.20: Isosurface rendering of the aortic arch of a patient with artificial aortic valve.

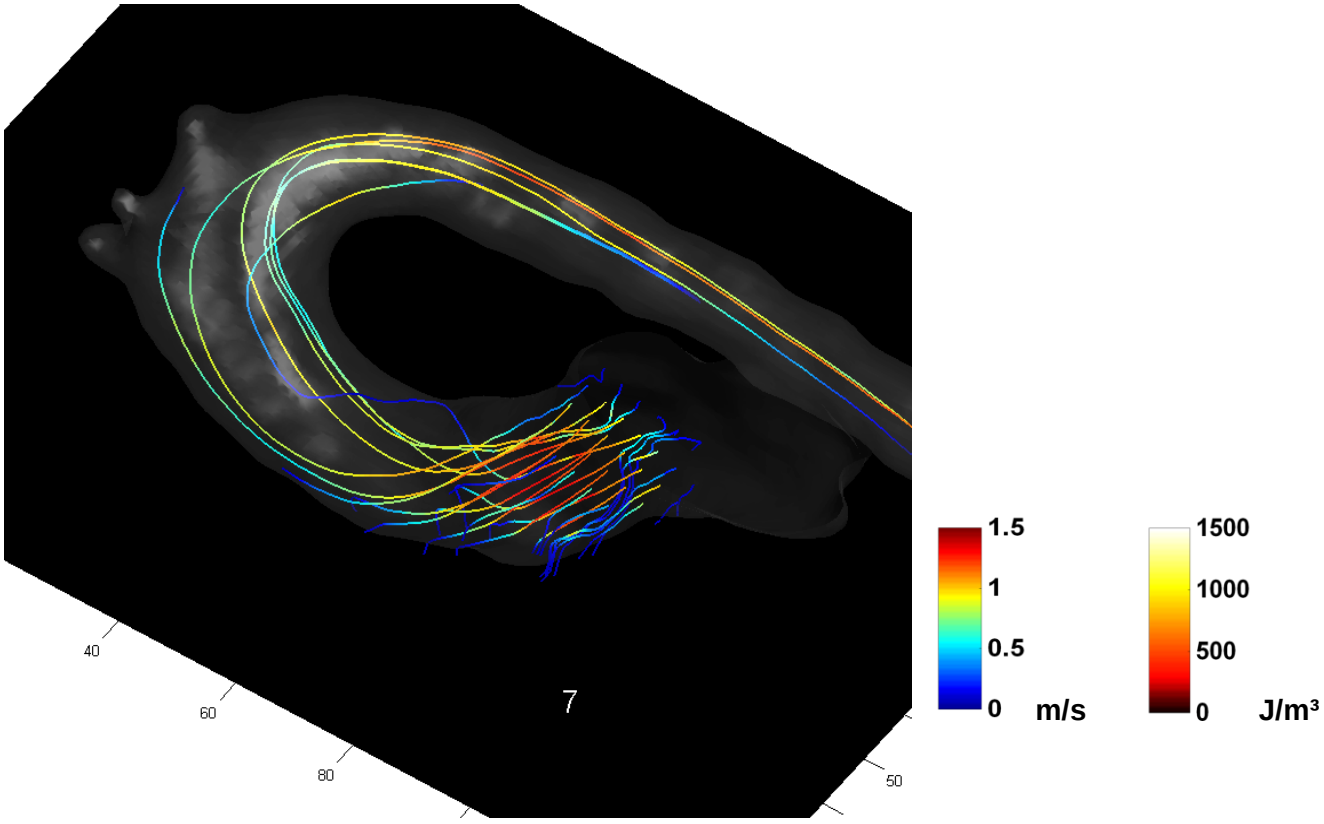

Fig. 3.21: Isosurface rendering of the aortic arch of a healthy volunteer. TKE values are smaller than 250 J/m³.

3.3.3 Particle Tracking

With in-vivo data, validation and comparison are more difficult than in-vitro as the true velocities are not known. No other imaging modality than MRI is able to provide a 3D velocity vector field. Using Doppler sonography, only special features like maximum velocity, or amount of flow can be compared.

A possibility to compare different datasets is particle tracking. Two regions of interest are selected, for example mitral and aortic valve, and pathlines are created. The percentage of particles reaching the second ROI (in terms of originating particles from the first) is noted and can be used as a relative measure of accuracy. Depending on the structure, different percentages can be expected – for a closed pipe or vessel it would be around 100%, for the heart 50-70% according to the physiological ejection fraction.

An example can be seen in Fig. 3.22, where the blue circle is the border of the mitral valve, and the red circle corresponds to the aortic valve.

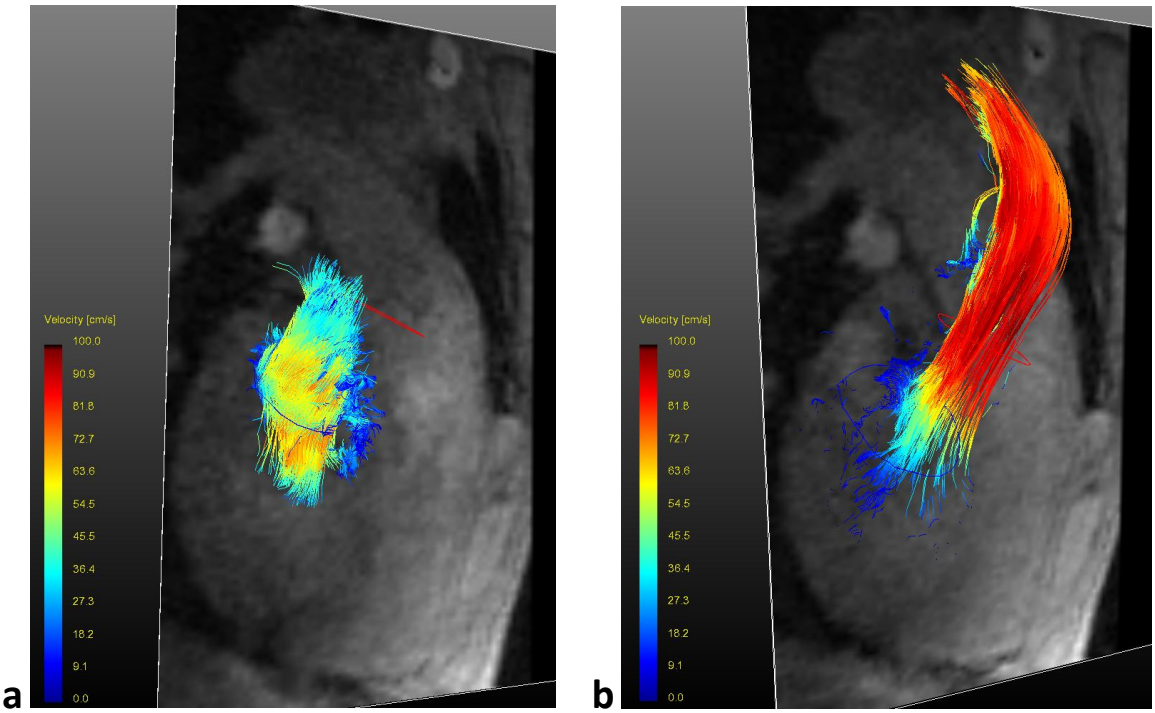

Fig. 3.22: Particle Tracking from a) the mitral valve during filling to b) the aortic valve at the end of systole. Note that the two ROIs were selected at different time points. The spatial relation not only results from the anatomy but also from the movement of the heart.

The results of two volunteers can be found in Table 3.2. These two were deliberately chosen to show the strongly varying absolute results between subjects, whereas the relative values of the individual techniques stay the same.

	2-point PC	**3-point PC**	**Bayes**
Volunteer 1	42.3 %	59.7 %	62.9 %
Volunteer 2	16.7 %	41.9 %	45.3 %

Table 3.2: Particle tracking results of two volunteers, comparing different velocity reconstruction techniques.

3.3.4 Discussion of the in-vivo results

The first challenge when trying to image flow up- and downstream of aortic valves arises from the lack of a standardized 2D view which depicts the ventricle as well as larger parts of the aorta. For the LVOT view used in this thesis, the aorta will be cut angulated downstream of the aortic valve. That is an issue especially when assessing post-valve turbulence, because the shear at the vessel wall will lead to an increase of the TKE values, and depending on the angle between plane and vessel wall the exact borders of the aorta cannot be detected.

Distinction between turbulence and shear at the vessel walls is not possible with the current algorithm. The detected “turbulence” at the vessel walls in Fig. 3.15 and Fig. 3.16 most probably results from shear effects leading to a high number of occurring velocities in a voxel. The relation of the thickness δ of the boundary layer to the diameter L and the Womersley number N_W is given by the equation $\delta = L/N_W$. Reported Womersley numbers for the ascending aorta range from 10 to 15 [34] leading to a boundary layer thickness of 2-3 mm. This corresponds to 1-1.5 voxels in our measurements. In 2D images the location of the vessel wall outside the imaging plane has to be known to distinguish between turbulence and shear. If additional points in k_v space are acquired, conclusions about the distribution of velocities in a voxel could be made. This approach is based on the model for a signal proposed by Dyverfeldt et al. [13], and will be subject to further investigations.

The comparison of the two patient cases clearly shows the benefits and drawbacks of artificial aortic valves. If conditions like cardiac output and geometry in patient 1 would be comparable to those in patient 2, a valve prosthesis would result in a significant reduction of

TKE and peak velocity. But still, an artificial valve cannot restore physiological flow conditions and the isosurface renderings show the large differences in flow pattern between patients and healthy volunteers.

The challenges in the measurements of pathological flow originate from either artifacts induced by the valve itself, or the high signal loss in very turbulent flows. Patient 1 also had a very distinctly curved aorta, making it hard to plan the imaging plane. Also the inter-subject variance of signal and SNR is quite large and hence a universally valid statement about the accuracy of the measurements is not possible. Another factor is the voxel size of 2 mm isotropic, which only allows a general assessment of the level of turbulence. If more information about the forces at the vessel walls is needed, the resolution has to improve as well.

Like the in-vitro results, particle tracking showed a higher performance of the Bayesian analysis than conventional methods in all volunteers. As can be seen in Table 3.2, 3-point PC encoding performed almost as well as the Bayesian method, and conventional 2-point PC is far behind. The scan times of the Bayesian approach and the 3-point PC are the same, as only 2 segments were used for this calculation. The 2-point PC scan would be about 40% faster though.

As a measure of quality, particle tracking has to be used with care, because of the high inter-operator variability. Especially in the heart it is difficult to determine the exact location of the valves, and parameters like the starting time point can severely affect the result. Therefore the method can be only used to compare different methods using the exact same data, where the parameters do not need adjustment. Another point to consider is the use of prospective triggering, where inevitable the late diastolic part of cardiac cycle is not imaged.

Despite these drawbacks, the results in the healthy volunteers were considered reliable. Up to 60% of the particles were exiting the left ventricle during the next heartbeat, which is in the range of the normal left ventricular ejection fraction of 50-70%.

4 Discussion and Outlook

In this work a method to determine flow velocity and turbulence intensity using phase-contrast (PC) MRI has been presented. Using Bayes' theorem, multiple measurements of velocity vector components are incorporated and hence information about velocity distributions becomes available. It is demonstrated that such a scheme permits measurements of mean velocity and turbulence intensity. It is also shown that many-point velocity-encoding offers improved precision compared to conventional 2-point approaches.

In simulations it has been shown that this technique benefits the most from additional measurements when having to deal with low SNR, a situation where averaging would lead to larger errors. By constraining the data to follow a given probability function, noise leads to a lower weighting of values which deviate strongly from other measured points. Therefore these quasi-outliers do not affect the result as severely as they would do when using conventional averaging. Assuming Gaussian noise, this principle also sets the number of required measurements in k_v-space in relation to the SNR. If the variance of the noise is high, a small number of measurements cannot compensate possible quasi-outliers. In chapter 3.1 it was demonstrated that the critical SNR value for a 3-point measurement is about three.

Comparisons between different methods may be biased by the choice of the error metric. The more outliers contribute to the result, the better the conventional 2-point PC measurement performs in comparison to the 3-point PC approach [14]. Irrespective these insights, the Bayes' method was found to outperform both the 2- and 3-point encoding schemes. The only exception was found in the high SNR regime, where the 3-point PC approach was found to perform slightly better than the Bayes' scheme when using an error metric insensitive to outliers.

The fact that the presented technique performs well at low SNR is advantageous especially for accelerated imaging application. This potentially enables higher acceleration factors and, accordingly, shorter scan times. The variable number of k_v steps also offers a finer trade-off between accuracy and speed as compared to conventional velocity encoding approaches.

In terms of user interaction, the Bayes' approach should also be more fault-tolerant than the 2-point PC measurement. In general, the maximum encoding velocity has to be higher than the maximum velocity occurring. However, because of the additional k_v steps, the exact choice will not affect the result as much as it would do in a 2-point measurement. This enables an implementation where a default and reasonable maximum encoding velocity would lead to acceptable results in a wide range of flow conditions. This fact also holds true for turbulence quantification and hence the method offers improved robustness relative to the previous method proposed for mapping turbulent kinetic energy [13].

In the analysis of artificial heart valves significantly higher TKE for found for the TAVI relative to the SJM design as a result of a single large flow jet. This jet was also noticeable in the in-vivo TAVI data. These results are, however, only of limited value to judge which valve to favor at the moment. The implantation of the SJM mechanical valve requires open heart surgery, which is not always feasible in older or weaker patients. Nevertheless, the higher durability of the mechanical valve makes it a preferred choice in younger patients.

Although a comparison between those two valves is difficult, the proposed method could help in improving the design of heart valves. To draw conclusions about the effects of different valve designs on flow characteristics, a study with several patients is necessary to eliminate the inter-patient variance. Such a study is planned together with clinical partners for the near future and will include a comparison of the Medtronics CoreValve and the Edwards Transcatheter Heart Valve.

A limiting factor for clinical use is the current processing time required by the Bayes' algorithm. Processing of a 3D scan of the left ventricular outflow tract (resolution 100x50x30) with 24 heart phases takes about 10 hours using standard computer hardware. There are several areas where the performance can be improved. All computations were performed in Matlab. The use of a more efficient programming language such as C as well as a customized optimization algorithm could allow a significant speed gain. Also the parameters used in the optimization algorithm (like the number of iterations or computational tolerance) can be adjusted to achieve an acceptable trade-off between speed and accuracy. It is also conceivable that a manual pre-selection of time points is performed and, for instance, only the ejection and the filling phases are reconstructed.

The method proposed in this work is not limited to the heart and aorta. It also lends itself well to examining different larger vessels of the circulatory system. Of particular interest are

flow patterns at branching points such as found in the carotid bifurcation, a site prone to the development of atherosclerosis. The application of the technique in smaller vessels may also be possible. Such an application would, however, demand improved spatial resolution of the measurement and hence prolonged scan times.

Another interesting application area concerns computation of relative pressures using the Navier-Stokes equation. By incorporating information about energy dissipation caused by turbulence, the accuracy of the results is expected to be further improved.

As the model of the effects of turbulence on the signal magnitude is based on an assumption about the characteristic time scales of turbulence, further validation of this method is required. To this end, a comparison of MRI and Particle Imaging Velocimetry (PIV) in a heart phantom is planned. Also further acceleration of the imaging process using radial sampling of k-space is currently being investigated. A low resolution and hence rapid approach using back projection may be devised, which would enable investigators to obtain a first overview of the maximum amount of turbulence occurring in patients.

In conclusion, this work has presented a novel approach to measure velocities and turbulence intensities in-vitro and in-vivo. Promising results regarding the accuracy compared to conventional methods have been presented with particular relevance in low SNR regimes. Accordingly, the method is expected to have considerable impact for image acceleration techniques which inherently compromise SNR for increased scanning speeds.

Feasibility of the method was demonstrated using in-vitro as well as in-vivo measurements, including pathological flow situations. In future work further investigation is needed to validate the results of turbulence intensities against a proven reference method.

5 References

[1] Petersen S, Peto V, et al.: European cardiovascular disease statistic. 2005 edition. *British Heart Foundation* (2005)

[2] Gill, RW: Pulsed Doppler with B-mode imaging for quantitative blood flow measurement. *Ultrasound Med Biol* 5(3): 227-235 (1979)

[3] Nerem RM, Rumberger Jr JA, Gross DR, Hamlin RL, Gleiger GL: Hot-Film Anemometer Velocity Measurements of Arterial Blood Flow in Horses. *Circ Res* 34: 193-203 (1974)

[4] Singer JR: Blood flow rates by NMR measurements. *Science* 130: 1652-1653 (1959)

[5] O'Donnell M: NMR blood flow imaging using multiecho, phase contrast sequences. *Med Phys* 12(1): 59-64 (1984)

[6] Srichai MB: Cardiovascular Applications of Phase-Contrast MRI. *AJR* 192: 662-675 (2009)

[7] Silverman JM, Raissi S., Tyszka JM, Trento A., Herfkens RJ: Phase-contrast cine MR angiography detection of thoracic aortic dissection. *Int J Card Imaging* 16: 461-470 (2000)

[8] Malek AM, Alper SL, Izumo S: Hemodynamic shear stress and its role in atherosclerosis. *JAMA* 282: 2035-2042 (1999)

[9] Hathcock JJ: Flow effects on coagulation and thrombosis. *Arterioscler Thromb Vasc Biol* 26: 1729-1737 (2006)

[10] Nyboe C, Funder JA, Smerup MH, Nygaard H, Hasenkam JM: Turbulent stress measurements downstream of three bileaflet heart valve designs in pigs. *Eur J Cardiothorac Surg* 29(6): 1008-1013 (2006)

[11] Kaminsky R, Kallweit S, et al.: PIV Measurements of Flows in Artificial Heart Valves. *Topics in Applied Physics* 112: 55-72 (2008)

[12] Gao JH, Gore JC: Turbulent flow effects on NMR imaging: measurement of turbulent intensity. *Medical Physics* 18(5): 1045-1051 (1991)

[13] Dyverfeldt P, Sigfridsson A, Ebbers T, Kvitting JPE: Quantification of intravoxel velocity standard deviation and turbulence intensity by generalizing phase-contrast MRI. *Magn Reson Med* 56: 850-858 (2006)

[14] Ringgaard S, Oyre SA, Pedersen EM: Arterial MR Imaging Phase-Contrast Flow Measurement: Improvements with Varying Velocity Sensitivity during Cardiac Cycle. *Radiology* 232: 289-294 (2004)

[15] Lee AT, Pike GB, Pelc NJ: Three-Point Phase-Contrast Velocity Measurements with Increased Velocity-to-Noise Ratio. *Magn Reson Med* 33: 122-126 (1995)

[16] Xing D, Gibbs SJ, et al.: Bayesian Analysis for Quantitative NMR Flow and Diffusion Imaging. *J Magn Reson, Series B* 106: 1-9 (1995)

[17] Hashemi RH, Bradley WG, Lisanti CJ: *MRI: The Basics.* 3rd Ed. Philadelphia, Lippincott Williams & Wilkins (2010)

[18] Johnson JB: Thermal agitation of electricity in conductors. *Phys Rev* 32: 97 (1928)

[19] Nyquist H: Thermal agitation of electric charge in conductors. *Phys Rev* 32: 110-113 (1928)

[20] Gudbjartsson H, Platz S: The Rician Distribution of Noisy MRI Data. *Magn Reson Med* 34: 910-914 (1995)

[21] Moran PR: A Flow Velocity Zeugmatographic Interlace for NMR Imaging in Humans. *Magn Reson Imaging* 1(4): 197-203 (1982)

[22] Bernstein, MA, King, KF, Zhou, XJ: *Handbook of MRI Pulse Sequences*. San Diego, Elsevier Academic Press (2004)

[23] Mathieu J, Scott J: *An Introduction to Turbulent Flow*. Cambridge, Cambridge University Press (2000)

[24] Grisworld, MA, Jakob, PM, et al.: Generalized autocalibrating partially parallel acquisitions (GRAPPA). *Magn Reson Med* 47: 1202-1210 (2002)

[25] Pruessmann KP, Weiger M, Scheidegger MB, Boesiger P: SENSE: Sensitivity encoding for fast MRI. *Magn Reson Med* 42: 952-962 (1999)

[26] Tsao J, Boesiger P, Pruessmann KP: k-t BLAST and k-t SENSE: dynamic MRI with high frame rate exploiting spatiotemporal correlations. *Magn Reson Med* 50, 1031-1042 (1993)

[27] Pedersen H, Kozerke S, Ringgaard S, Nehrke K, Kim WY: k-t PCA: temporally constrained k-t BLAST reconstruction using principal compenent analysis. *Magn Reson Med* 62: 706-716 (2009)

[28] Giese D, Knobloch V, Schaeffter T, Pedersen H, Kozerke S: Spatio-temporally constrained reconstruction for highly accelerated flow MRI. *J Cardiovasc Magn Reson* 12 (Suppl 1): 73 (2010)

[29] Bretthorst GL: Bayesian Analysis. I. Parameter Estimation Using Quadrature NMR Models. *J Magn Reson* 88: 533-551 (1990)

[30] Jeffreys H: An invariant form for the prior probability in estimation problems. *Proc R Soc Lond A* 186(1007): 453-461 (1946)

[31] Bretthorst GL: Bayesian Analysis. IV. Noise and Computing Time Considerations. *J Magn Reson* 93: 369-394 (1991)

[32] Stadlbauer A, van der Riet W, Globits S, Crelier G, Salomonowitz E: Accelerated Phase-Contrast MR Imaging: Comparison of k-t BLAST With SENSE and Doppler Ultrasound for Velocity and Flow Measurements in the Aorta. *J Magn Reson* 29: 817-824 (2009)

[33] Kvitting JPE, Dyverfeld P, et al.: In Vitro Assessment of Flow Patterns and Turbulence Intensity in Prosthetic Heart Valves Using Generalized Phase-Contrast MRI. *J Magn Reson* 31: 1075-1080 (2010)

[34] Fung YC: *Biomechanics: circulation*, 2nd Ed. New York, Springer Verlag (1996)

List of Figures

List of Tables

Acknowledgements

I wish to express my sincere gratitude to Prof. Sebastian Kozerke for giving me the opportunity to work on this interesting topic, his guidance and patience. His expertise and helpful advice was a key factor in the making of this work.

I also would like to thank Prof. Dr. Rudolf Stollberger for agreeing to supervise this thesis on behalf of the University of Technology Graz and his patience.

This thesis would not have been possible without the invaluable assistance, continuous support and helpful suggestions of Verena Knobloch, for which I am deeply grateful.

On the same occasion, I would like to extend my gratefulness to all members of the MR cardio group for all their informative discussions. Further I would like to thank all members of the IBT MR group for providing such a wonderful working environment.

I would also like to thank my family for their wonderful support all throughout my studies.